Article

Severe Wildfires Near Moscow, Russia in 2010: Modeling of Carbon Monoxide Pollution and Comparisons with Observations

Alexander N. Safronov *, Ekaterina V. Fokeeva, Vadim S. Rakitin, Eugene I. Grechko and Roman A. Shumsky

Obukhov Institute of Atmospheric Physics, Russian Academy of Sciences, Pyzhevskii per. 3, Moscow 119017, Russia; E-Mails: efokeeva@ifaran.ru (E.V.F.); vadim@ifaran.ru (V.S.R.); grechko@ifaran.ru (E.I.G.); shumsky@ifaran.ru (R.A.S.)

* Author to whom correspondence should be addressed; E-Mail: safronov_2003@mail.ru; Tel.: +7-495-953-3762; Fax: +7-495-953-1652.

Abstract: The spatial and temporal distributions of the carbon monoxide (CO) concentration were calculated with the Regional Atmospheric Modeling System and Hybrid Particle and Concentration Transport model (RAMS/HYPACT) in the provinces near Moscow during the abnormally hot summer of 2010. The forest, steppe and meadow hot spots were defined by the satellite data MCD14ML (MODIS Terra and Aqua satellite data). The calculations indicated that the surface CO concentrations from the model were two times less than the experimental data obtained from the Moscow State University ataset. The M and Zvenigorod Scientific Station (ZSS). Conversely, the total column CO concentrations obtained from the model were two to three times larger than the experimental values obtained from the Obukhov Institute of Atmospheric Physics (OIAP) and ZSS stations. The vertical transfer of pollutants was overestimated. Tentatively, it could be assumed that an aerosol influence in the model calculations is a reason for the overestimation. The comparisons between the wind speed, temperature and humidity profiles calculated in the model with the data from the standard balloon sounding exhibited good agreement. The CO total column data of the Measurements of Pollution in the Troposphere (MOPITTv5 NIR and TIR/NIR) obtained from the OIAP and ZSS stations appear more realistic than do the MOPITTv4 data. However, the surface MOPITT values of CO concentration for Moscow have the large distinction from the ground measurements.

A careful proposal regarding satellite orbit optimization was made, which could improve future spectrometric measurements, such as the MOPITT, Atmospheric Infrared Sounder (AIRS) and Infrared Atmospheric Sounding Interferometer (IASI) measurements.

1. Introduction

The abnormally hot summer of 2010 in European part of Russia was characterized by the extended absence of precipitation. This drought led to a reduction of water fractions in grassland and tree leaves. Low moisture in moss, lichen and grassland vegetation leads to favorable conditions for the rise and fast propagation of bottom wildfires in forests and in grassland. Alternatively, a reduced water table in the soil of bog systems stimulates peat fires. First, a bottom wildfire becomes a surface peat fire, and then it becomes an underground peat fire near tree roots and stems, see [1,2]. It is worth noting that peat fires have occurred regularly in the Moscow region; for example, peat fires were reported in the summer of 2002 (e.g., [3,4]).

Various concentrations of CO, CO_2, VOC (volatile organic compounds), CH_4, NO_x, NH_3, and SO_2 gases and PM_{10} and $PM_{2.5}$ aerosols were detected in atmosphere the atmosphere during forest, steppe and peat wildfires [5]. Wildfire emission nearby Moscow in the summer of 2010 were studied by a number authors, see [6–14]. In these studies, the wildfires nearby Moscow have been investigated by different methods such as by using a balance method, forward and reverse modeling. In particular, the uncertainty of wildfire emissions due to using the various vegetation maps could be found in our previous study [15].

Carbon monoxide is known as a pollutant that can be (along with aerosols) a good indicator of all burning processes. Because the atmospheric lifetime of CO varies between two weeks and three months (depending on the season), it is convenient to use this pollutant to study the transport processes.

The fires in the summer of 2010 near Moscow have brought to light a number of problems.

First problem was concerned the fact that the AIRS (Atmospheric Infrared Sounder) [16], MOPITT (Measurements of Pollution in the Troposphere) [17], and IASI (Infrared Atmospheric Sounding Interferometer) [18] satellite sensors have low sensitivity to pollutants in the lower troposphere up to approximately 2 km in altitude. A comparison between data from the MOPITTv4, AIRS and IASI with the ground-based total column data obtained from the OIPA (Obukhov Institute of Atmospheric Physics) and MSU (Moscow State University) stations was presented in previous studies [4,6]. However, the MOPITT multispectral technique has been applied to improve the sensitivity of the MOPITT (see about the MOPITT v5 in [19] and [20] and about the MOPITT v6 in [21], March 2013). At the beginning the sensibility of the new MOPITTv5 NIR channel was checked. Analysis of new NIR channel measurements pushed us to think about solving this problem by "lift-up" filtering.

The second aspect revealed during a discussion of the fires near Moscow concerns the accuracy of the fire emissions inventories. In this study, our approaches to CO emission estimations were compared with the estimations obtained by using inverse modeling [7]. Below we discuss in detail the results of [7] that used the TM5-4DVAR method to recreate the emissions from the IASI and MOPITTv4 satellite data.

The third problem is a part of a global problem to the transition from the operational monitoring of atmospheric pollution (*i.e.*, from the recording of a current status of air pollution) to the operative forecast of atmospheric pollution (*i.e.*, to prediction of atmospheric air quality). The absence of the really operating atmospheric pollution prediction system had a very negative impact on the population of the Moscow region during the fires in 2010. A statistical analysis [22,23] showed that the cumulative excess of mortality in July and August 2010 equals 54,000 deaths if compared to the same period in 2009. Excess deaths in the regions were caused by extreme heat and a large quantity of carbon monoxide in atmosphere. Thus, developing of the forecasting air quality system is import task for saving lives in megapolysis.

This study represented the complex comparative analysis of performed measurements in the column and in the surface layer of atmosphere with the satellite data and results of modeling simulations.

2. Data, Model and Approach

2.1. Surface CO Measurements

The surface carbon monoxide (CO) concentration measurements presented in this study were detected with the automated infrared absorption gas filter correlation instrument TE48S instrument (Thermo Electron Corp., Waltham, MA, USA [24]). It allows for measuring background CO mixing ratios at a level of less than 100 ppb with the total uncertainty of ±10 ppb. The data was collected in Moscow at the observation station through the organized effort of the Geographical Faculty of the Moscow Lomonosov State University (MSU, 55.707°N, 37.523°E) and the Obukhov Institute of Atmospheric Physics (OIAP, Russian Academy of Sciences, 55.739°N, 37.623°E) and outside of Moscow at the Zvenigorod Scientific Station (ZSS, 55.738°N 36.882°E, located 53 km west of Moscow).

2.2. Total Column CO Measurements

Two similar spectrometers, based on a homemade diffraction grating monochromator with a 0.2 cm^{-1} spectral resolution and equipped with a solar tracker, were used for spectroscopic measurements in the downtown area of Moscow on the roof of the OIAP building and at the ZSS station outside of Moscow.

The carbon monoxide total column (TC) was retrieved from an absorption spectrum in the infrared spectral range (2153–2160 cm^{-1}) [25,26], using a standard nonlinear least-squares procedure [27,28]). This algorithm was realized by calculating the HITRAN-2000 parameters of the absorption lines, the standard vertical profiles of interfering gases such as O_3, N_2O, and CO_2, the balloon sounding temperature and the water vapor profiles. For the calculations from the periods without fires period, the standard CO profile (named CO NCAR) was used. This profile is same that is used in MOPITT v3 processing [29]. This CO profile has a ground concentration equal 120 ppb, with decreasing concentration with height

to 80 ppb at the tropopause level. In our retrievals during the fire period, we used a modified CO profile with CO ground concentrations obtained at the MSU and ZSS stations and an AIRS CO concentration profile for heights of 3 km and greater for each day of measurements.

2.3. Satellite Measurements

In the near infrared, the satellite sensor sensitivity to contaminants in the lower troposphere is low, as was shown again during the investigation of the wildfires in 2010 near Moscow [6]. The comparisons of CO total column ground-based measurements obtained from the OIPA and ZSS stations with MOPITTv4, AIRS and IASI satellite data were published previously, see details [4,6]. In this study, we turn our attention to a new multispectral data processing algorithm derived from the Terra/MOPITT (MOPITTv5) sensor. The new multispectral CO retrieval MOPITTV5 products were based on simultaneous observations of a thermal-infrared (TIR) band near 4.7 μm and near-infrared (NIR) band near 2.3 μm. The details were published in [19,20].The V5 TIR-only and NIR-only CO retrieval products are also available in MOPITTv5. As described in [20], the MOPITT V5 NIR is available only in clear-sky daytime scenes over land. However, the MOPITT multispectral TIR/NIR product is available for all scenes (day/night, land/ocean). The retrieval exploits only the TIR channels. Note that the MOPITT Version 4 (V4) product is based exclusively on the TIR observations [30]. The daily grid products with Level 3 NIR (MOP03N, version L3V3.1.2), TIR (MOP03T, version L3V3.1.1) and combined TIR/NIR (MOP03J, version L3V3.1.3) that were available on the server [31] were used in this study.

The Terra and Aqua satellites pass over the OIAP station twice a day. The MODIS/Aqua is characterized as day/night sensor due to the Aqua overpass the station at 12:30–16:00 LT and at 02:30–05:00 (next day) LT. In contrast, the MODIS/Terra sensor is characterized as a morning/evening sensor due to it overpasses the station in intervals of 13:30–14:00, 21:30–01:30 LT (next day).

According to the MODIS data, between 1 June 2010 and 1 September 2010, 14,725 and 12,330 fires were detected by the Terra and Aqua satellites, respectively. In case of Aqua the 6653 hotspots were recorded in a daylight time and 5677 hotspots were registered in a nightlight time. Therefore, the relation of daylight to nightlight registration numbers is equal 1.17. In case of Terra, out from 14,725 hot spots the 5728 fire ignitions were identified in the morning and 8997 fire ignitions were registered in the evening.

2.4. Meteorological Model Regional Atmospheric Modeling System (*RAMS*)

The Regional Atmospheric Modeling System/Hybrid Particle and Concentration Transport (RAMS/HYPACT) model [32] is typically used for modeling the transport processes of passive compounds (such as Noble gases), or small active chemical compounds (such as CH_4 and NH_3) and aerosols on a regional scale (in the range of 100 m to 1000 km). The basis for using this model was the fact that the transport time of pollution from the hot spots to Moscow (~1.5–2 days) is shorter than the carbon monoxide life time (~10 days) [33].

An analysis of the RAMS model meteorological field quality was performed. The model meteorological field parameters were compared with the sounding data from the World Meteorological Organization (WMO) stations #27612 (Dolgoprudnyj, below DOL) and #27730 (Ryazan, below

RYA). The RYA station (54.63°N, 39.70°E, 158.0 m a.s.l.) was located near the major peat fires, while the DOL station (55.75°N, 37.95°E, 200 m a.s.l.) was located in the suburb of Moscow.

The RAMS (Regional Atmospheric Modeling System) is a non-hydrostatic regional model for simulating and forecasting meteorological phenomena [34–36]. The RAMS is based on the numerical solution of the original equations of atmosphere dynamics with additional parameterizations for turbulent diffusion, forward and backward solar radiation scattering, precipitation, orographic effects, convection processes, water vapor and heat fluxes from soil surfaces, trees canopies and water surfaces (model LEAF3) (see for more details [36]). The tree domains with 4-fold zoom resolutionsand with cell size of 50 km, 12.5 km and 3.125 km were used in this study (see Figure 1a–c).The domain dimensions were $100 \times 100 \times 30$, $42 \times 42 \times 30$ and $30 \times 30 \times 30$ cells, respectively. The first domain covered almost all of the European part of Russia, the second domain covered the region of the wildfires near Moscow, and the third domain covered the Moscow megalopolis borders of 2010.
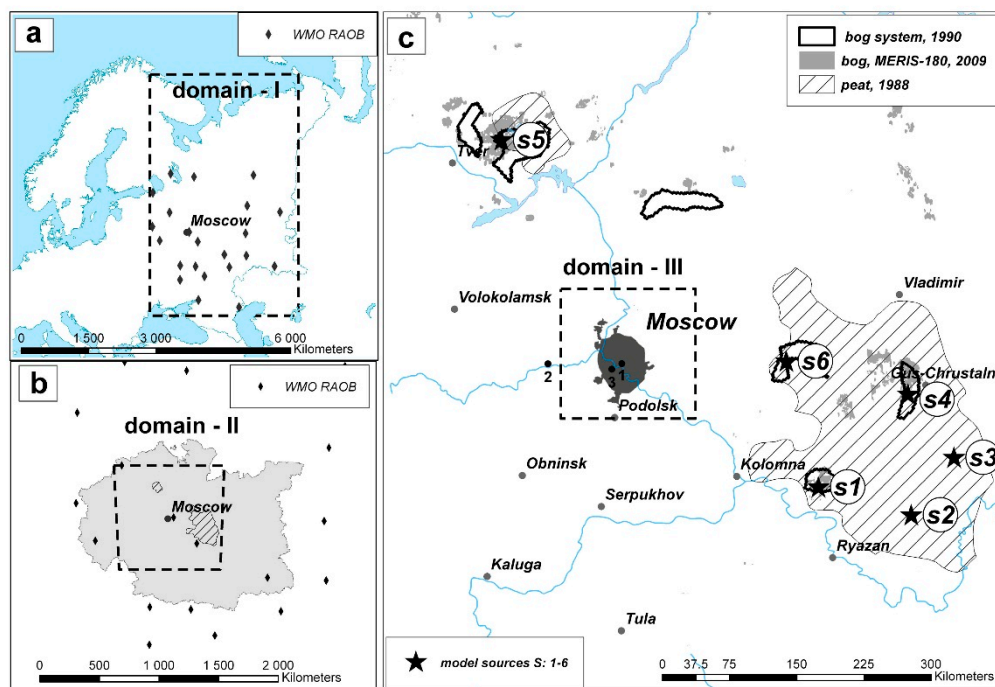

Figure 1. Three Regional Atmospheric Modeling System (RAMS) domains are shown in (**a**), (**b**) and (**c**) frames. The outer counter (grey area) around of Moscow is corresponded to area with the intensive wildfires (b). The locations of 22 WMO upper air stations (WMO RAOB) are shown in (a,b). The bog system and peat are in the central part of Russian plain (c). The three scientific stations are shown: 1—OIPA, 2—MSU, 3—ZSS (c). The major places of localization peat wildfires are specified in (c) as s1–s5 stars.

All the model calculations were produced for the entirety of the heat wave that occurred between the 1 June 2010 and 1 September 2010. The σ_z coordinate system was used in the RAMS model. In that system, the top layers are flat, and the bottom layers follow the contours of the relief.

The simulation used 30 layers in the σ_z coordinate system, which was set irregularly in the vertical direction from the earth surface to the height of approximately 20 km. The bottom layers increased in height by a factor of 1.15, so the first 11 layers comprised the lower 2 km of altitude.

The reanalysis of the DS083.2 meteorological fields (NCEP FNL Operational Model Global Tropospheric Analyses) [37] with a resolution of 1° × 1° at 6-h intervals was used for the initial and boundary conditions.

The topography in the domains was at 30 s resolution [38]. The average orography was used because the height of the topography along the plume tracks was less than 300 m. The sub-model LEAF3 (The Land Ecosystem-Atmosphere Feedback model, [39]), which takes into account the soil types, snow coverage, vegetation classes, *etc.*, was used for the estimation of the water vapor and heat fluxes from the surface.

A simple radiation model [40] was used in the shortwave and longwave spectral ranges. In this radiation scheme, the processes of coagulation and condensation for cloudy systems were considered. The time step of calculations under the radiation scheme was 600 s.

The Kuo scheme [41] was used for simulating convective processes in the first and second domains. We did not simulate the convection in the third domain because there is no any scheme which is appropriate for the coarser resolution. The time step of the calculation under the convection scheme was 1200 s.

The microphysical parameters demanded by the model were included. The microphysics in RAMS includes the treatment of cloud water, rain, pristine ice, snow, aggregates, graupel and hail. For a detailed description of the RAMS microphysical—precipitation scheme see [35,42]. The diameters of raindrops, snowflakes, mixed particles, and graupels were calculated by the prognostic equation for each category.

Atmospheric turbulence was considered under the Smagorinsky scheme [43] in the horizontal direction and under the Mellor-Yamada level 2.5 scheme [44,45] in the vertical direction.

The lateral boundary conditions were entered according to the Klemp-Wilhelmson scheme [46] for the normal velocity component of the east and west boundaries. These boundary conditions are intended to allow the most disturbances to propagate out of the model domains without a strong reflection. The top layer appeared as a rigid layer with high viscosity, and the gravity waves were dumped.

The initialization level was determined by using the ISAN (ISentropic ANalysis) sub-model, which is hybrid of the isentropic, σ_z and surfaces analyses [32,47,48]. The isentropic analysis was carried out with a time interval of 6 h at 43 levels for two domains in the middle and upper troposphere.

2.5. Dispersion Model

The Hybrid Particle and Concentration Transport (HYPACT) model is the dispersion model for calculations of the temporal and spatial distributions of gaseous admixtures and aerosol particle concentrations [49]. The model allows both the Lagrangian and Eulerian calculation methods and, in addition, the hybrid approach, which uses the Lagrangian particle method at short distances that is then transformed into Eulerian concentrations [50]. The Eulerian principle of plume calculation was used in the present study. The HYPACT dispersion model works with the RAMS meteorological fields, and we also used RAMS fields with the radiation, convective, advection, microphysics schemes, *etc.*, described above (see Section 2.4).

The HYPACT model was used to estimate the air quality and to test the emission scenarios in studies at both regional and local scales. Examples of HYPACT model applications can be

found in [51–58]. Unfortunately, it is not possible to take in account the radiation balance changes induced by a large amount of wildfire aerosol in the current RAMS/HYPACT model version.

2.6. Meteorological Data Assimilation

At a preliminary stage of the research a weak correlation between the calculated wind RAMS fields and the sounding data was defined, so the RAMS observational data assimilation methods (ODA) were used. The locations of the 22 WMO sounding stations, which provide atmospheric profiles every 12 h for ODA procedure, are shown in Figure 1a.

Two different observational data assimilation procedures might be used in RAMS. One uses the observations in a data analysis procedure in ISentropic Analysis (ISAN) to modify the first-guess fields (in model initialization stage). The other nudges the model fields to the data observations during an assimilation procedure (in model calculation stage). For increasing the reliability of simulations, we used data assimilation procedures at both of these stages.

The first ODA procedure (sometimes called analysis nudging) typically uses as a first guess field reanalysis data (DS083.2 in the present study) and uses as an additional option radiosonde data. Note that there are four layers in the ISAN methods (see also [59]). The hybrid analysis between the isentropic and σz datasets is accomplished in the layers above 4 km andunder 6 km (mix layer). For layers lower than 4 km, the data were obtained completely from the σz analysis; for layers above 6 km, the data are from the isentropic analysis. In this study, the surface data analysis is also blended with the σz analysis in a layer from the ground to 1 km. The gridded pressure data were taken as a first guess field, and the observations were objectively analyzed and applied to this first guess field as deviations in this study. The influence analysis nudging extends inward from the lateral boundary of the model domain by five grid cells.

The second ODA procedure (sometimes called observation nudging) has an impact on several parameters: the horizontal components of wind speed, the potential temperature, the non-dimensionalized pressure (Exner function) and the total water mixing ratio. The influence spreads inside of areas with a radius of 100 km in the upper air analysis for domain-I. For 12 hourly upper air observations, the interpolation and extrapolation times for the kriging procedures in the ODA scheme were equal to 12 h and 6 h, respectively.

3. Emission Scenarios

3.1. Emission Schemes

In this study, two methods were used to estimate the fire emissions.

A typical procedure (below it is called as "bulk" method) was applied for the estimation of CO emission by using the following equation [5]:

$$Emission = A \times B \times CE \times EF \tag{1}$$

where *A*—burned area; *B*—fuel loading, kg/m^3; *CE*—fraction of biomass fuel burned; *EF*—CO emission per kg biomass burned, g/kg.

The fuel loading and emission factor that depended on burned vegetation types, were taken from the original work [5]. The vegetation map description could be found in Section 3.4. Uncertainties that related to different land cover maps using were discussed early in [15].

Also in this study, the method based on the Fire Radiation Power (FRP) [60] method was applied for the estimation of CO emission for comparison with other results. The CO emission calculation in FRP method was made using the next general formula:

$$Emission = K \times Q \times EF \tag{2}$$

where $Q = 0.368$ FRP (MW); Q—burning speed, kg/s; $k = 86400$—coefficient of transformation, s/day.

3.2. Hot Spot Localization

In this study, three MODIS products (MOD14, MYD14 Level 2 and MCD45) were used to locate the sources of ignitions.

First, the location of hot spots was defined with the MCD14ML (Global Monthly Fire Location Product) dataset provided by the University of Maryland (University of Maryland, Department of Geography, ftp-server fuoco.geog.umd.edu, [61]), which includes hot spot positions, pixel temperatures on mid-wavelength infrared T21 (3.929–3.989 microns) and T31 (10.780–11.280 microns) channels, FRP and confidence of hot spot detection. The MODerate resolution Imaging Spectroradiometer (MODIS) can routinely detect both flaming and smoldering fires ~1000 m^2 in size. Meanwhile, the operational orbital products MOD14/MYD14 MODIS (Level-2) were rapidly obtained using the "Active Fires" method (below AF), "an IR-method of recording the total count of hot spots and a estimation of fire areas" [62–64].

The Level 2 product is defined in the MODIS orbit geometry, which covered an area of approximately 2340 by 2030 km in the across- and along-track directions, respectively. As known from [64] under very good observing conditions (e.g., near nadir, no smoke, relatively homogeneous land surface, *etc.*) flaming fires of 100 m^2 in size can be detected. For details see also [62] and the MODIS website [65].

In our study, the hot spots presented as point sources, and emissions from the Terra and Aqua satellites were estimated separately. According to the MODIS data, 14,725 and 12,330 fires were detected by the Terra and Aqua satellites, respectively, between 1 June 2010 and 1 September 2010.

Second, the location of hot spots was defined by using "Burned Areas" technology (below BA). In some publications (e.g., [66]), the estimation of CO emission for the purpose of climatology was already made by using BA technology (product MODIS—MCD64A1). The MCD64A1 product was developed by Giglio *et al.* (see for details [61]).

However, in this study the other BA MODIS product namely MCD45A1/C5 collection was used. Its detailed description can be found in [67,68]. The difference between the spatial distribution of wildfires, obtained by AF (Figure 2a) and BA, MCD45 (Figure 2b) methods was shown for an example of peat fires near "s1" location (see also the legend of the Figure 1c) for a period of intense smoke in Moscow metropolis. It is clear from data presented in Figure 2a,b that the AF method gives higher amount of ignition sources than the BA method does. However, most of these AF wildfire spots correspond to the low-temperature ignition with FRP <100 MW.
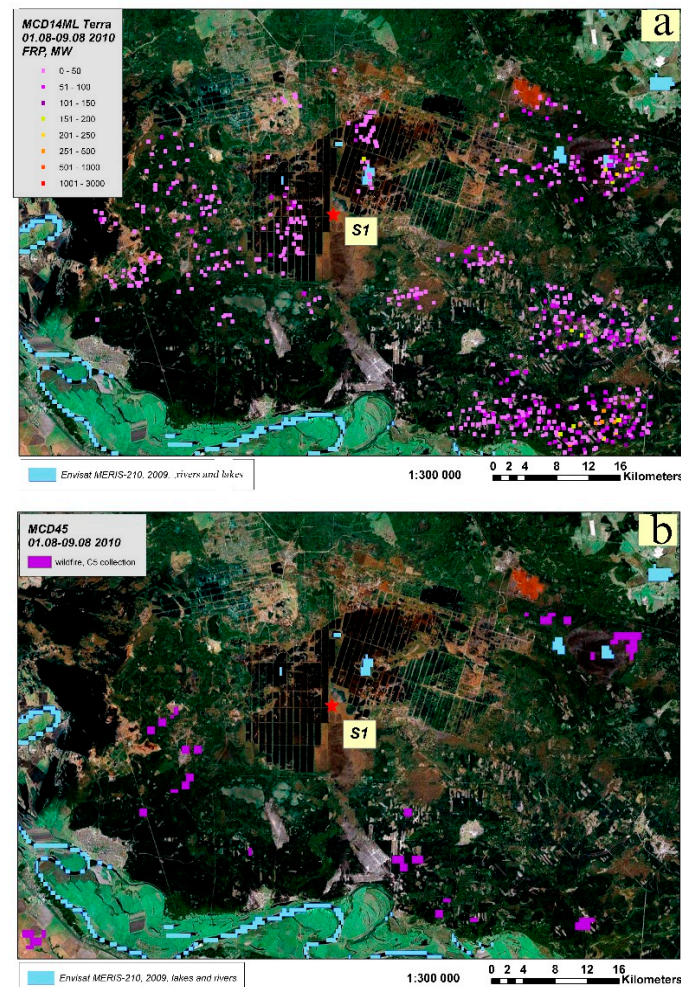
Figure 2. The spatial distribution of MCD14ML (**a**) and MCD45 (**b**) hot spots on the peat land were illustrated on GoogleEarth satellite photos. This peat location in European Russian plain is shown in Figure 1c as "s1" red asterisk. The dark squares indicate the peat mining. The drainage systems appear as blue color lines between the dark squares. The water surface as a map layer was added according to Envisat/MERIS–210 satellite data at 2009 year status. The hot spot locations, which were obtained during temporal period from 1 August to 9 August 2010, by MODIS/Terra satellite data (MCD14ML, method AF), are displayed in (a) as different color points, graduated by FRP values. To compare the wildfire localizations by using the AF method and by the BA (MCD45) method, the areas burned during the temporal period from 1 August to 9 August 2010 are shown in (b).

Our previous studies have shown that most of the hot spots had low FRP values, so in most cases, forest surface fires, peat fires, steppe, and grassland were observed. However, increased values of CO emissions appeared as a result of incomplete fuel burning, *i.e.*, high values are typical for burning of wood mulch, wet grass, or scorched areas, (see also discussions in [69–72]). Therefore, it was assumed that the effective injection height of the plume was low and was set to 50 m in our calculations.

The detailed comparison between of different remote sensing products: MOD14/MYD14, MCD45A1 and MCD64A1 (GFED3.1) is presented below in the Discussion section.

3.3. Duration of Hot Spot Burning

It is assumed that the fire begins at the moment of the registration by the satellite and the fire proceeds until the moment of the next overpass. The satellites pass over specific geographical points twice per day, so for simplicity it was considered that the hot spot burns during approximately the 11 h after the moment of its registration by the satellite. Within such approach it was assumed that the ignition was absent if the wildfire pixel from space was shielded by clouds or heavy smoke.

Note, that the MCD14ML dataset was a derivative of the MOD14/MYD14 product and, just as MOD14/MYD14, contained a precise time of the fire pixel burning.

Also note that the MCD45A1 product gives burned pixels with a resolution of 500 m as the Level-3 product for a month. The "Burned Areas" technology is not operational (the data are accessible with a considerable delay). Alternatively, there is only "approximal Julian day of burning" included in the MCD45A1 dataset, so this dataset cannot be used for forecast AQ system. However the MCD45A1 dataset was suitable only as a part of emission submodel for reanalysis air quality system.

3.4. Vegetation Map Global Land Cover 2000 (GLC-2000)

The emission factor(EF) depends on the type of burnt vegetation, which is defined by the vegetation map. The Global Land Cover 2000 (GLC-2000) vegetation map created on the basis of the SPOT-4 satellite data was used in the present study. This map covers a time interval from January 2000 to December 2000 and has a spatial resolution of 1 km. For details, see [73,74] and the Global Land Cover 2000 database description [75].

The wide-angle, low-resolution VGN ("VEGETATION") sensor installed on SPOT-4 (Satellite Pour l'Observation de la Terre, abbreviation in French) satellite has 4 channels, each of which works in a specific range of frequencies and covers the total angle of vision. The spectral bands for the VGN channels were as follow: in the visible range Green/B1 (0.50–0.59 microns), Red/B2 (0.61–0.68 microns), in the near infrared range NIR/B3 (0.78–0.89 microns) and in the infrared range MIR/B4 (1.58–1.75 microns). The total viewing angle of the VGN sensor was 101°, which provided a capture belt 2250 km wide. The optimum pixel size for the channels of the VGN sensors is 1.165×1.165 km.

The GLC-2000 vegetation area calculation was made on the basis of the S-10 images received from the SPOT-4/VGN sensor. The classification of the vegetation types was made using the relation of the NIR/RED and NIR/MIR channels for the individual images in the absence of snow and cloud cover.

The peat bogs are placed into the category of regularly flooded bushes and meadows (GLC-15) and are partially taken into account in the emission sub-model ($B = 7.55$ kg/m^2, $CE = 0.46$, $EF = 89$ g/kg). For peat fires, B depends on the thickness of the burnt peat layer, CE is close to 1 and the emission factor (EF) is 210 g/kg [76,77].

3.5. Peatlands

The marshy systems were identified using a ground-based vegetation map [78] and a satellite-based vegetation map. "Regularly flooded territories" (land cover class 180) of the Medium Resolution Imaging Spectroradiometer Instrument [79] GlobCover product were used. Algorithms of this product are better adapted for decoding vegetation of European Russian plain. The peat soil layer was the same

as [80]. The marshy systems [78,79] and peat [80] are shown in Figure 1. The example of peatland structure was shown in Figure 2 as a high resolution satellite image on which the fire hot spots from MODIS sensor are marked.

Due to a fact that the basic process of peat burning occurs under the surface we decided to use heated smoke exuding from soil as a source of the hot spot identification. As a result all values of hot spot confidence (MODIS AF parameter) including values of the low confidence (~30% of total) were involved. The using of the FRP method (Equation (2)) as calculation method for underground peat burning estimation is disputable.

3.6. Section Summary

The calculation of emission is an independent part of this study which was carried out before a start of dispersion model simulation. The emissions were obtained by using two calculation schemes (bulk method based on Equation (1) and FRP method based on Equation (2)) and by using three ignition localization schemes (MOD14, MYD14 and MCD45). The received emissions were also compared with inventories (FINNv1, GFEDv3.1 and GFASv1). These results are presented below in the Discussion section (see Table 1).

As an emission submodel for RAMS/HYPACT simulation it was used a bulk method (Equation (1)) as a calculation scheme and were used two schemes of hot spot localizations: MOD14 (Terra) and MYD14 (Aqua).

4. The Results of the RAMS/HYPACT Model Calculation and Wildfires in Russia in 2010

4.1. The Results of the Meteorological Field Calculation

The accuracy of dispersive model results is depended in many respects on the accuracy of the meteorological field calculations. The analysis of RAMS meteorological fields is shown in this section.

The quality of the RAMS meteorological fields was estimated by comparison to the meridional and zonal winds. In addition, a comparison of the sounding datasets ([81]) to the vertical profiles of wind, temperature and relative humidity that were obtained from the DOL and RAY stations was carried out. We compared the RAMS meteorological field parameters to balloon data for the entire hot summer period, but, we will focus on launches at 00:00 and 12:00 UTC on 5 August 2010, and 7 August 2010.

Typically, meteorological balloons supply data at heights from 200 m to approximately 18,000 m. However, the balloon of 7 August 2010, 12:00 UTC, reached a height of only 14,277 m (~142 hPa) and supplied measurements on 50 levels. The RAMS wind profiles (the module of speeds in a horizontal plane) and the sounding data from the DOL and RAY stations are presented in Figure 3a,b as solid dark lines and circles, respectively. The comparison of simulated and experimental results has shown that changes in the meridional and zonal wind are in agreement with the model on 5 and 7 August 2010. The correlation coefficient (R), bias (B) and standard deviation (SD) for simulated and sounding data are also shown in Figure 3a,b.

Table 1. Total CO emission from wildfires in the central part of Russian plain (grey area in Figure 1b) between 1 July and 1 September 2010, calculated by different methods. The emission values of fire at peat areas (hatch areas in Figure 1c) and their percentage are specified. The emissions, calculated in this study are highlighted.

Emission Inventory		CO, 1 July 2010–1 September 2010				Possibility to be Used in Forecasted AQ System
Localization of Ignitions	Calculated by Method	Central Part of Russian Plain, Tg	Peat Area, Tg	Difference, Tg	Peat/Total, %	
MOD14	FRP (Equation (2))	2.27	0.79	1.48	34.8	√
MYD14	FRP (Equation (2))	1.85	0.66	1.19	35.7	√
MCD45A1	Bulk (Equation (1))	5.76	1.19	4.57	20.7	--
MOD14	Bulk (Equation (1))	35.32	13.58	21.74	38.4	√
MYD14	Bulk (Equation (1))	29.29	12.13	17.16	41.4	√
Other Emission Inventories						
FINNv1		2.56	0.87	1.69	34.0	
GFEDv3.1		1.53	0.45	1.08	29.4	--
GFASv1		11.07	8.37	2.7	75.6	
TM5-4DVAR Inversion Modeling Result with before/after Assimilation the IASI Data						
GFED3 [*]		0.63/10.06		--		
GFAS [*]		10.52/9.93		--		--

[*] definition of the R1 region see in Section 5.2.

A significant difference between prediction and measurements was observed on 7 August 2010 00:00 UTC, at the RAY station at 900 hPa. The deviation of the modelled speed from the values obtained by the balloon amounted to 6 m/s (at 950 hPa). The quality of the plume calculations strongly depends on the quality of the meteorological field calculation up to 850–900 hPa.

The B, R and SD from 20 July to 20 August did not show any peculiarities. For example, the correlation (R) between the simulated wind speed values and the sounding data was 0.60, and the bias (B) was 0.99 for the DOL station. The statistical calculation included 1060 points. When we used the values below 800 hPa, the R was 0.63, and the bias was 0.96 (from 448 points).

The accuracy of the dispersion model simulation, in addition to the wind parameters, strongly depends on the vertical mixing, which is depressed by a temperature inversion in the near-surface layer at night. Thus, during the night all pollutions from surface emission sources were trapped in the 300–400 m layer, and as a result, the concentrations of pollutions were raised in inversion layer.

To investigate a behavior of inversion layer, the microwave remote sensing of PBL (Planetary Boundary Layer) temperature profile by single-channel MTP-5 radiometer (Microwave Temperature Profile) was applied [82]. The MTP-5 data (0–600 m) from the MSU station are presented in Figure 4a. The experimental sounding and RAMS simulated temperature profiles are also shown in Figure 4a,b. The balloon data detect the temperature inversion because a balloon provides points of measurements below heights of 500–600 m. Therefore, according to the Dogloprudnaja-27612 and MTP-5 station data, the inversions were observed on 5 and 7 August 2010, at 00:00 UTC (local time 04:00). It can be concluded that the RAMS model poorly describes the night inversions in this special case (see Figure 4a,b). Note that the high correlation coefficient (R ~ 1.00) between RAMS simulation and

sounding data was calculated for the entire troposphere (1000 hPa–100 hPa). The correlation, bias and standard deviation, which are presented in Figure 4a,b as R, B, and SD, were calculated for the lower troposphere (below 750 hPa).
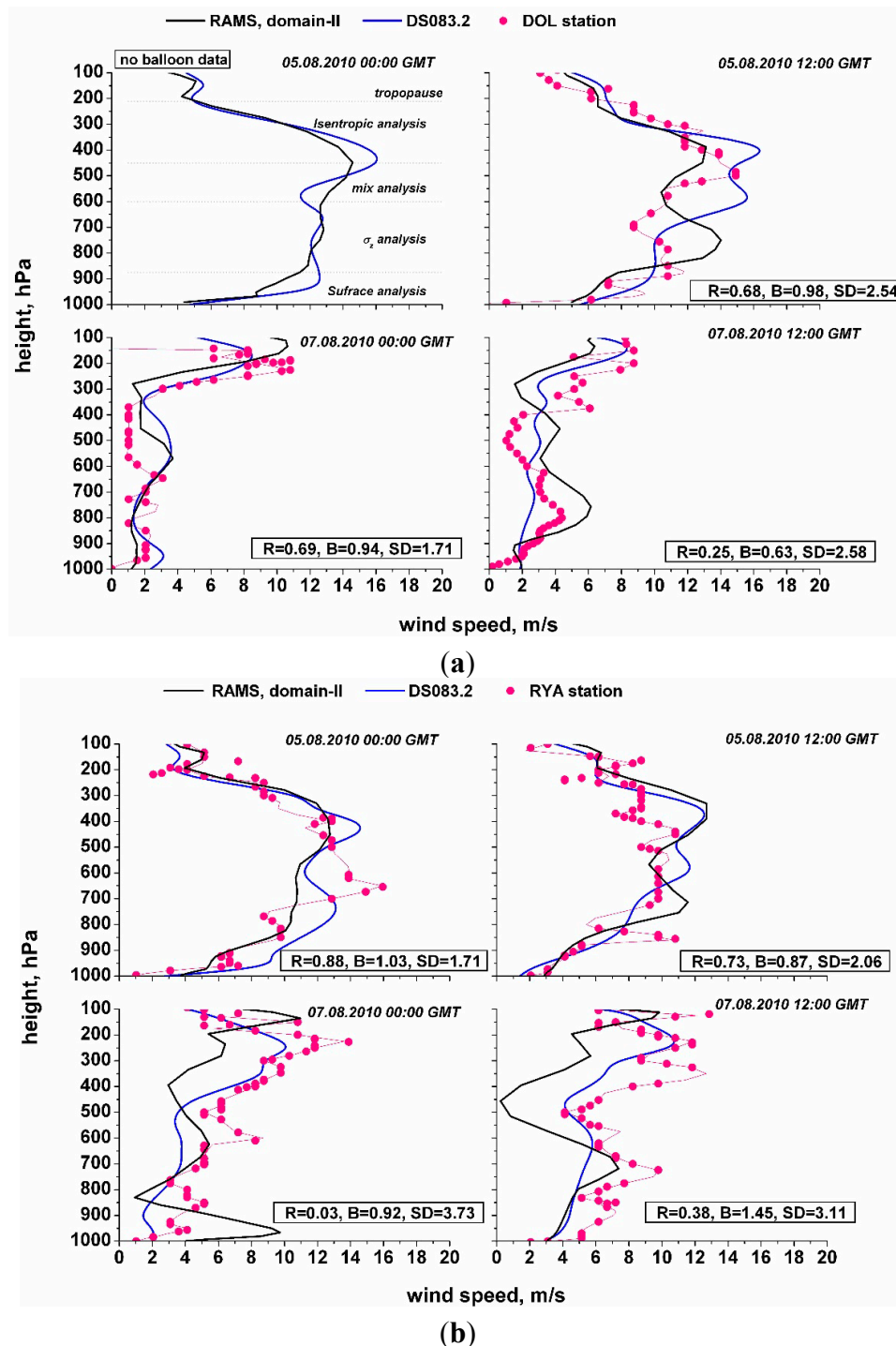

Figure 3. (**a**) Experimental (balloon at DOL station) and model (RAMS/HYPACT for the domain-II) wind profile (wind speed in the horizontal plane). The input of the DS083.2 meteorology field with resolution 1° × 1°, which was used as model initial and boundary conditions, is shown with thin grey lines. The analysis nudging (ODA) elements and the tropopause are marked in (**a**) (5 August 2010); (**b**) Same as for Figure 3a, but for RAY station.

Strong oscillations in the temperature profile below 850 hPa were recorded at the RAY station sounding data (see Figure 4b). These oscillations may be related to the presence of a dense mass of aerosol in the air. Let us note that our research group does not carry out our MTP-5 measurements near Ryazan, so we cannot confirm the fidelity of these measurements. However, according to MODIS satellite data, the huge amount of aerosols was detected near Ryazan at this time.
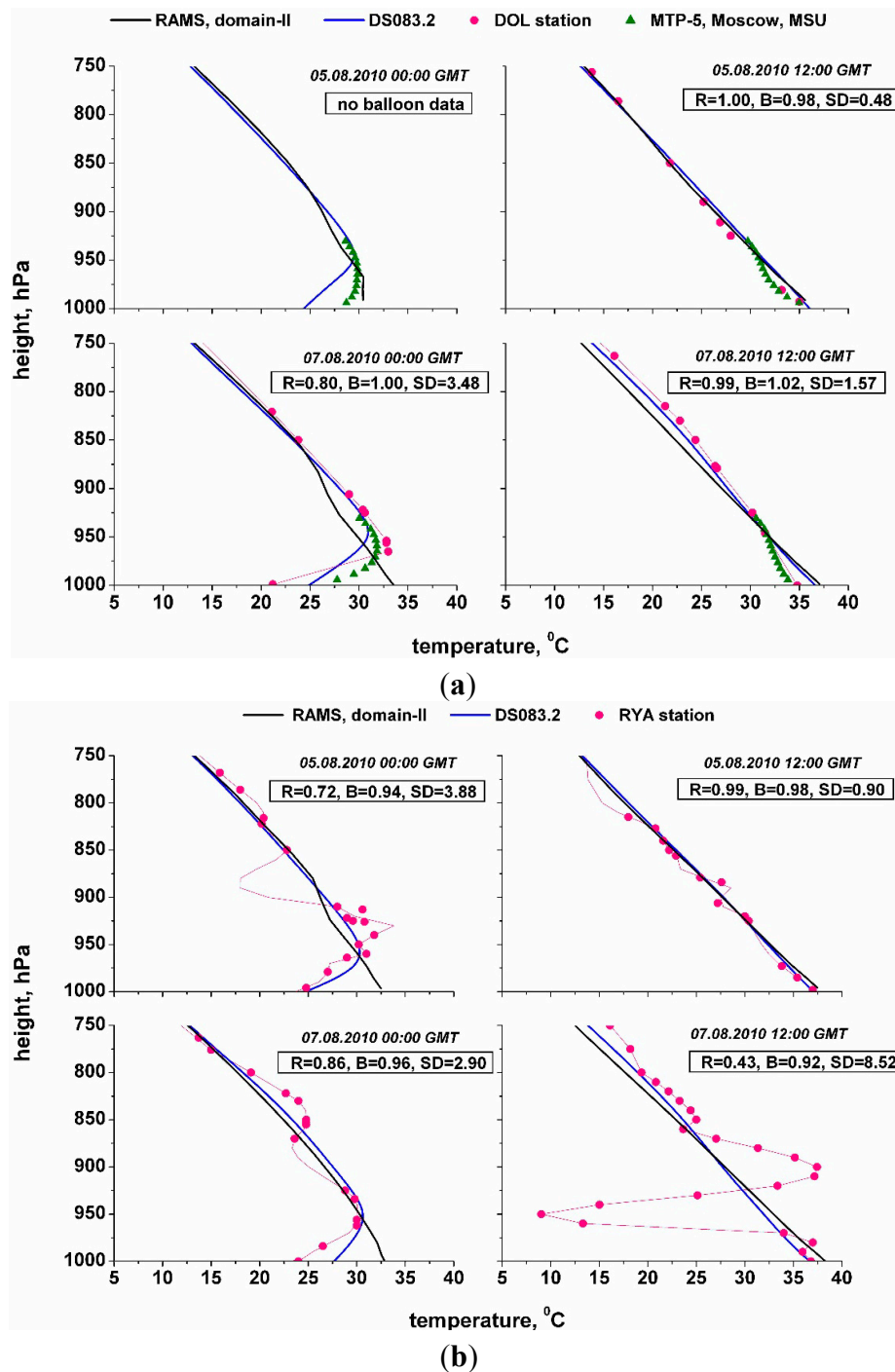

Figure 4. (**a**) Experimental balloons (DOL station) and model (RAMS/HYPACT for the domain-II) temperature profiles. In addition the MTP-5 experiential data from MSU station have been shown; (**b**) Experimental balloons (RAY station) and model (RAMS/HYPACT for the domain-II) temperature profiles.

The observed abnormally behaviors of temperature inversion were recorded during all period of extended aerosol presence in Moscow. The morning and evening inversions abnormally exceeded 11 h on 25, 26, 28, and 29 July and on 6–9 August 2010. The late destruction of the inversions, which started at 11–12 h (LT), and the absence or extremely late start of the evening inversions were also recorded. Such effects are rare in these latitudes in summer [8]. However, during the period of atmospheric blocking without the presence of aerosols in the atmosphere (July 2010), the inversions were not observed at all from 1 till 17 July 2010. The only exception was the inversion at 10 July 2010; the duration of this inversion was 4:15 h. As a rule, the height of these inversions did not exceed 300–400 m. Thus, the MTP-5 data obtained at the MSU station shows a strong suppression of vertical mixing in the near-surface layer.

Of course, the absence in 2010 the scientific research drones, allowing to investigate the atmosphere parameters in all PBL (0–4 km), did not allow us to make a clear conclusion about the suppression of vertical mixing in all volume of PBL. However, up to level 600 meters, this conclusion is justified.

A comparison of the PBL height calculated with the RAMS model and the PBL from the GDAS (Global Data Assimilation System) meteorological field is shown in Figure 5 (NOAA archive server, [83]). We used the 3-h ARL GDAS data at 1° × 1° horizontal resolution. As shown in Figure 5, both the RAMS and the GDAS data overestimated the PBL height in the period of intensive wildfires. Note that in case that the PBL height exceed the 2 km level, the MOPITT, AIRS and IASI sensors would easily detect pollution in the lower troposphere.
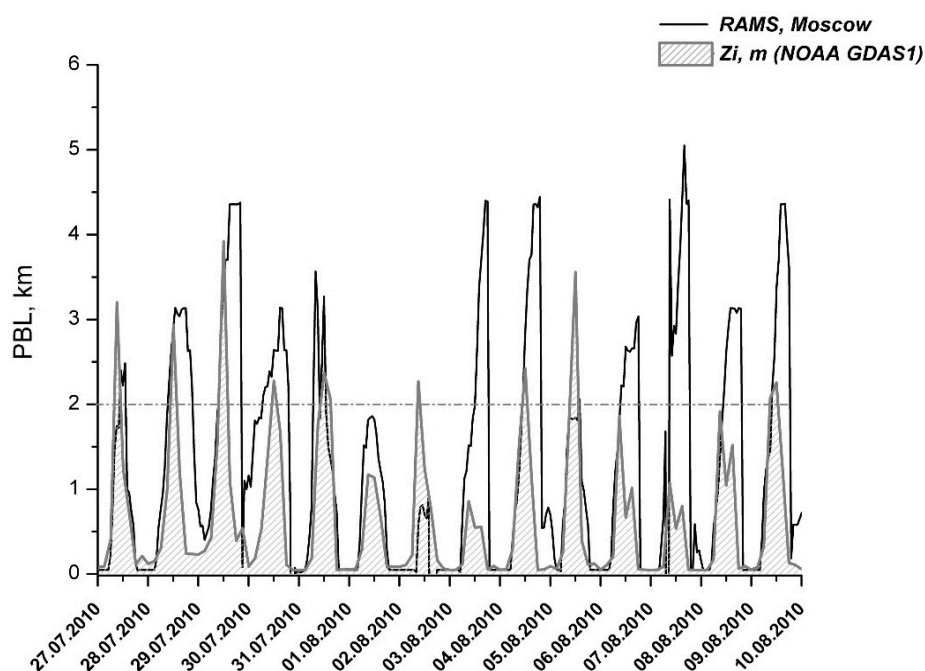

Figure 5. The planetary boundary layer height calculated by RAMS model and from NOAA GDAS meteorological fields.

Carbon monoxide is removed from the atmosphere as a result of its reaction with the OH radical. The vertical profiles of relative humidity are plotted in Figure 6, and the balloon data were in agreement with the predicted values. Low air humidity (<40%–50%) was found between the surface and a height of 850 hPa. The low air humidity and the minimal air mass transport time from the major

peat fires to the research sites in comparison to the CO lifetime allowed us to neglect the CO reaction with OH in this study [36]. The humidity profiles for the RAY station look similar.
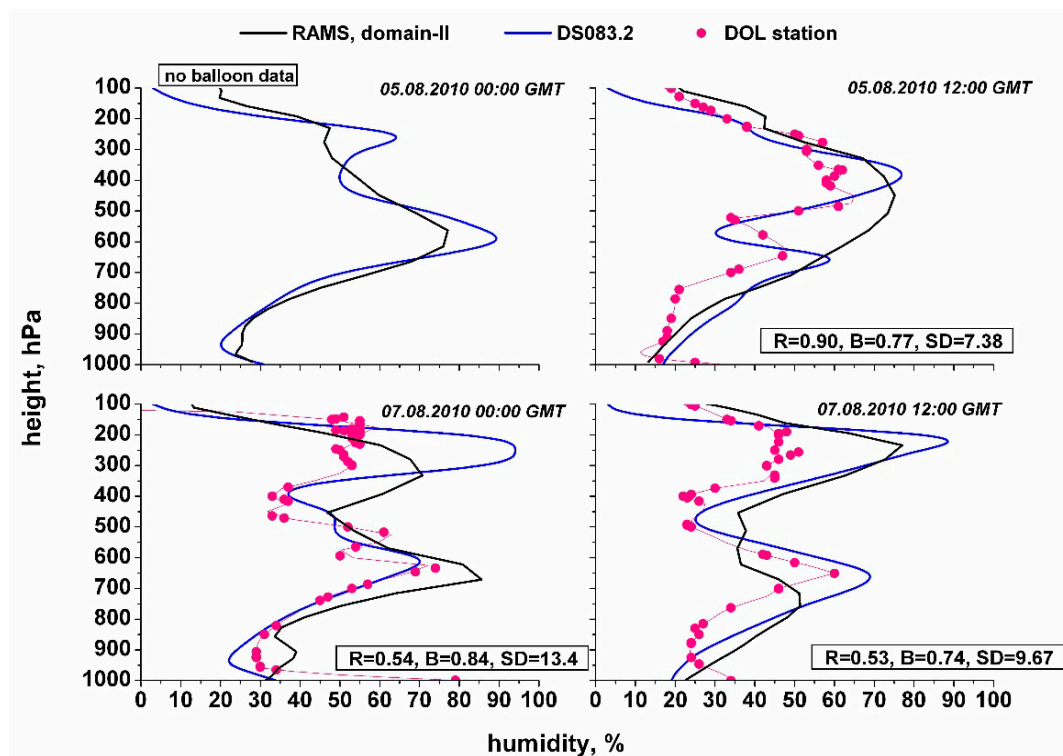

Figure 6. Experimental (balloons at the DOL station) and model (RAMS/HYPACT for the domain-II) humidity profiles.

4.2. Analysis of the Spatial Distribution of Wildfire Plumes

The RAMS/REVU ([84]) and GrADS ([85]) packages were used for the visualization of the model results between 20 July 2010 and 20 August 2010. However, these packages were not designed for full-scale geoinformation systems, so the full-scale GIS system ArcInfo ([86]) was also used.

In addition, the results of the visualization by ArcInfo allowed the display of the auxiliary information on a map derived from other sources, e.g., from megacity contours, residential areas, hydrology, settlements, *etc.* (Figure 7a,b).

The spatial distribution of CO concentration averaged over two hours at the height of 155.5 m a.g.l., on 8 August 2010, 09:00 UTC, for two model domains is presented in Figure 7. For these domains, the concentration scales are different. For the second and third domains, it begins with 1000 $\mu g/m^3$ with different steps.

As demonstrated in Figure 7a, the plume from the forest and peat fires reached Moscow, and the carbon monoxide concentration on 8 August 2010, 09:00 UTC, in the northeastern area of Moscow (~5000 $\mu g/m^3$) was one half the concentration in the southeastern area (~10,000 $\mu g/m^3$).
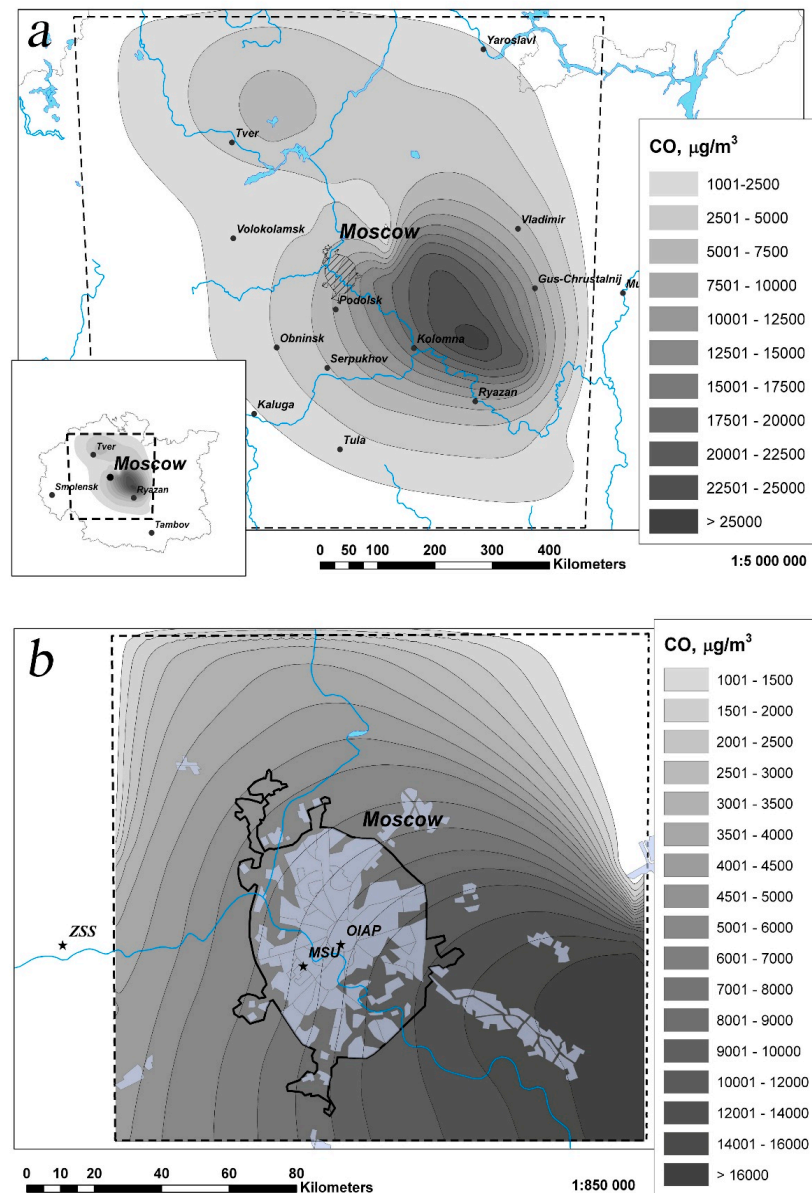
Figure 7. The spatial distribution of CO near Moscow at height of 155.5 m a.g.l., 8 August 2010 9:00 UTC, the domain-II (**a**) and domain-III (**b**) RAMS/HYPACT (Terra hot spots). Scale for CO starts at 1000 μg/m³. The dashed line corresponds to the domains. In addition the residential areas and the city contour (as it is in 2010) are shown in (b). The positions of observational stations are marked as stars in the third domain (b).

The detailed distribution of the CO concentration over the megalopolis on 8 August 2010, 09:00 UTC, is presented in Figure 7b for the third model domain. As shown in Figure 7b, the concentrations from the MSU and OIPA stations are located approximately on the same isoline (~7000–8000 μg/m³) whereas the concentrations from the ZSS station are in the range of 2500 to 3000 μg/m³.

During this period, the CO concentration in southeastern Moscow, near the Moscow Belt Highway (MBH), was approximately 10,000 μg/m³, which could be compared to the data in Podolsk, however in northwestern Moscow, the CO concentration was approximately 5000 μg/m³. The detailed comparison of the RAMS/HYPACT model results with the observations is shown and discussed below.

4.3. Comparison of Model CO Concentrations with the Experimental Data from the Moscow State University (MSU) and Zvenigorod Scientific Station (ZSS)

The concentrations of CO calculated by the model at heights of 100 and 500 m a.g.l are presented in Figure 8a,b for the MSU and ZSS stations, respectively. The data were obtained by the projection of the spatio-temporal distribution of concentrations on the station positions using the standard interpolate feature of RAMS/REVU [84]. The solid and dashed curves on the figures show the carbon monoxide concentrations, calculated using the hot spots detected by the MODIS/Terra and MODIS/Aqua, respectively. The grey areas are the experimental data.

As shown in Figure 8a,b, there are differences in the model results with emission based on the two satellite data sets (solid—Terra, dashed—Aqua), but the general trends of concentration changes are common during the hot summer period.

The comparison of the model results for the different height levels (Figure 8a,b) has shown that the amplitude of the peaks decreased and the plots became smoother when the height increased. However, the maximum concentrations for all levels between 6 August 2010 and 10 August 2010 are 3 to 4 times lower than the experimental data. Single peaks on 29 and 30 July 2010, and 11 and 12 August 2010 were not recorded at the MSU station (Figures 8a). The simulation results for ZSS station (Figures 8b) looked better; however in this case the model surface concentration was underestimated as well as for all period of intensive wildfires.
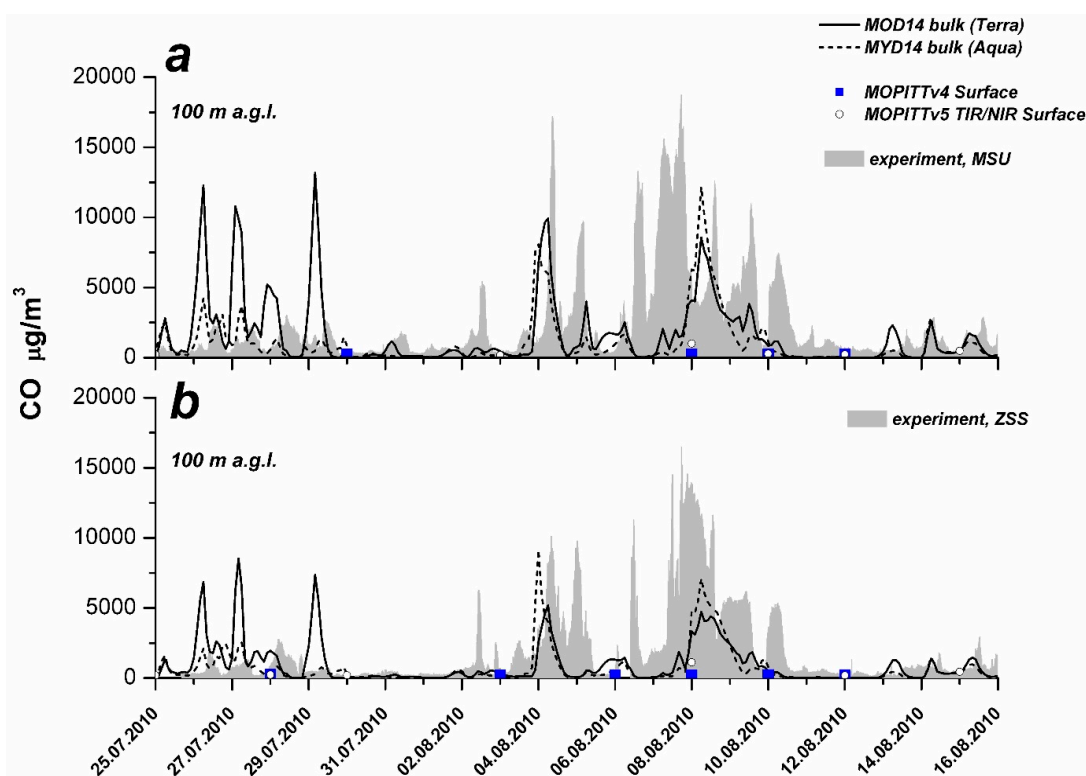

Figure 8. Experimental data for MSU (**a**) and ZSS (**b**) stations and model RAMS/HYPACT CO concentrations, at heights of 100 m a.g.l. The concentrations have been predicted by the model with using of the MOD14 (Terra, solid line) and MYD (Aqua, dashed line) bulk methods. The grey areas correspond to the experimental data. In addition surface CO concentrations of MOPITTv4, MOPITTv5 TIR/NIR satellite data are shown.

In summary, only a qualitative agreement between the results of the RAMS/HYPACT simulations with the surface measurements at the MSU and ZSS stations can be reported. It is happened due to the fact that the model does not account for the impact of aerosols on atmospheric processes, in particular the model overestimates the turbulent mixing in the lower troposphere. The model, with the wildfire emission sub-model described above, underestimates the carbon monoxide concentration near the ground layer by 3–4 times. A quantitative modeling of wildfires will require significant improvement in the models.

The surface CO concentrations of the satellite data: MOPITTv4, TIR channel and MOPITTv5, TIR/NIR channels are also shown in Figure 8a,b. The total amount of MOPITT surface concentration points is not enough (in a range from 3 to 6), and any of MOPITT surface values did not reached 1000 $\mu g/m^3$. At the moment of maximum pollution in the megalopolis basin, the surface satellite data showed values that are more than 10 times lower than the ground-based concentration measurements.

4.4. Comparison of Model CO Total Columns with Experimental Data from the Obukhov Institute of Atmospheric Physics (OIAP) and Zvenigorod Scientific Station (ZSS)

The comparison of the simulated and experimental results for the CO total column is shown in Figure 9. The background experimental values are not shown in this figure. It is clear from the curves that unlike surface concentration, the RAMS/HYPACT model values of CO total column are overestimated for the OIAP and ZSS stations by at least 2–3 times. Moreover, the predicted value does not explain the increase of CO total column on 3−5 August 2010.

Thus, only qualitative agreement between the RAMS/HYPACT model calculations and the total column measurements at the MSU and ZSS stations was found. The RAMS/HYPACT model with the wildfire emission sub-model described above overestimated the column values by 2–3 times.
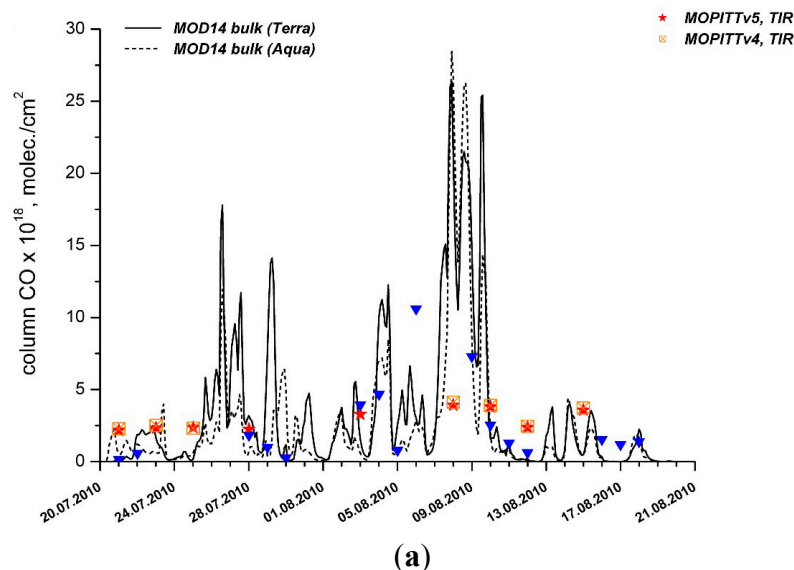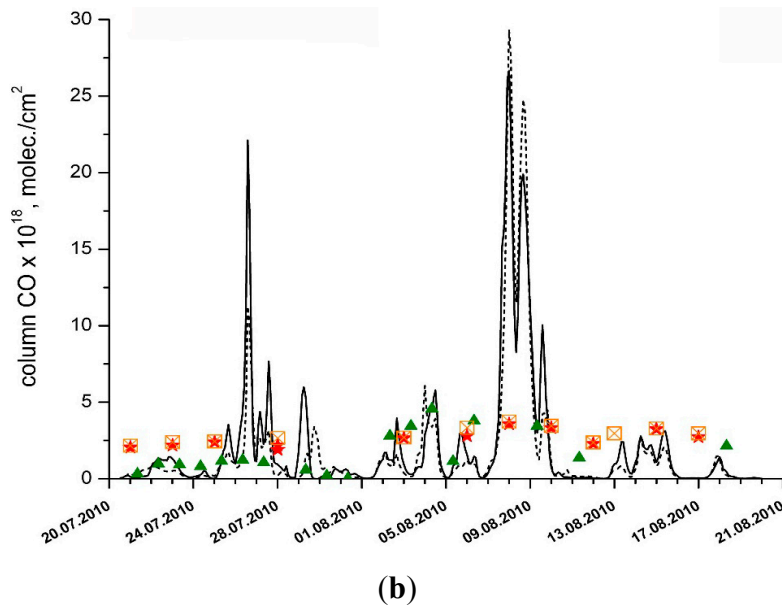

(a)

Figure 9. *Cont.*

(b)

Figure 9. Experimental for OIAP (**a**) and ZSS (**b**) stations and model (RAMS/HYPACT) CO total columns. The model CO total column has been obtained for the hot spots, predicted by MODIS/Terra satellite (solid line) and MODIS/Aqua satellite (dashed line). The triangles in the plot indicate the exceeding of experimental values over background. The MOPITTv5 TIR-only and MOPITTv4 satellite data have been shown as circle and cross correspondingly.

4.5. A Comparison of CO Total Column Measurements with the MOPITTv4 and MOPITTv5 Data

The satellite sensors have low sensitivity to gaseous pollutants in the lower troposphere. In 2012, the MOPITT-Team introduced a new MOPITTv5 product, which has been obtained by using a new additional spectral NIR channel, as well as a combination NIR and TIR channels. It is interesting to compare the CO total columns measured at the OIAP and ZSS stations with the new satellite products. The comparison between the MOPITTv5 TIR-only and MOPITTv4 (TIR) with the CO total column is shown in Figure 9a,b. The MOPITT data were received from cells of the nearest stations. Significant differences between the MOPITTv4 and v5 TIR channels were not revealed. The sharp distinctions between the MOPITTv4 and experimental CO total column values for OAPI and ZSS were discussed earlier in [4,6].

The comparison of the new MOPITT products, such as MOPITTv5 NIR-only and MOPITTv5 TIR/NIR, and the experimental OIPA and ZSS data were more interesting (see Figure 10a,b). As you can see from Figure 10a,b, significant differences between the MOPITTv5 NIR-only and multispectral MOPITTv5 TIR/NIR products were not observed. However, the increased values for both of these new products in comparison with TIR MOPITTv4 look promising. This slight excess indicates that the MOPITT sensor is alive, but the sensitivity of this sensor for all channels is strongly suppressed in the low troposphere.

Thus, for the OIPA station, the MOPITT TIR/NIRCO total column on 8 August 2010 was 5.38×10^{18} molec/cm^2, while the total column of the MOPITTv4 was only 4.125×10^{18} molec/cm^2. The total column for the ZSS station location was 5.52×10^{18} molec/cm^2, from the MOPITT TIR/NIR

product and 5.03×10^{18} molec/cm^2 from the MOPITT NIR-only product. These values are greater than 3.74×10^{18} molec/cm^2, which was obtained from the MOPITTv4 dataset. Recall that the MOPITTv4 uses only the TIR channel. We note that the amount of TIR/NIR data was less than amount of MOPITTv4 data during the period shown in the figures.
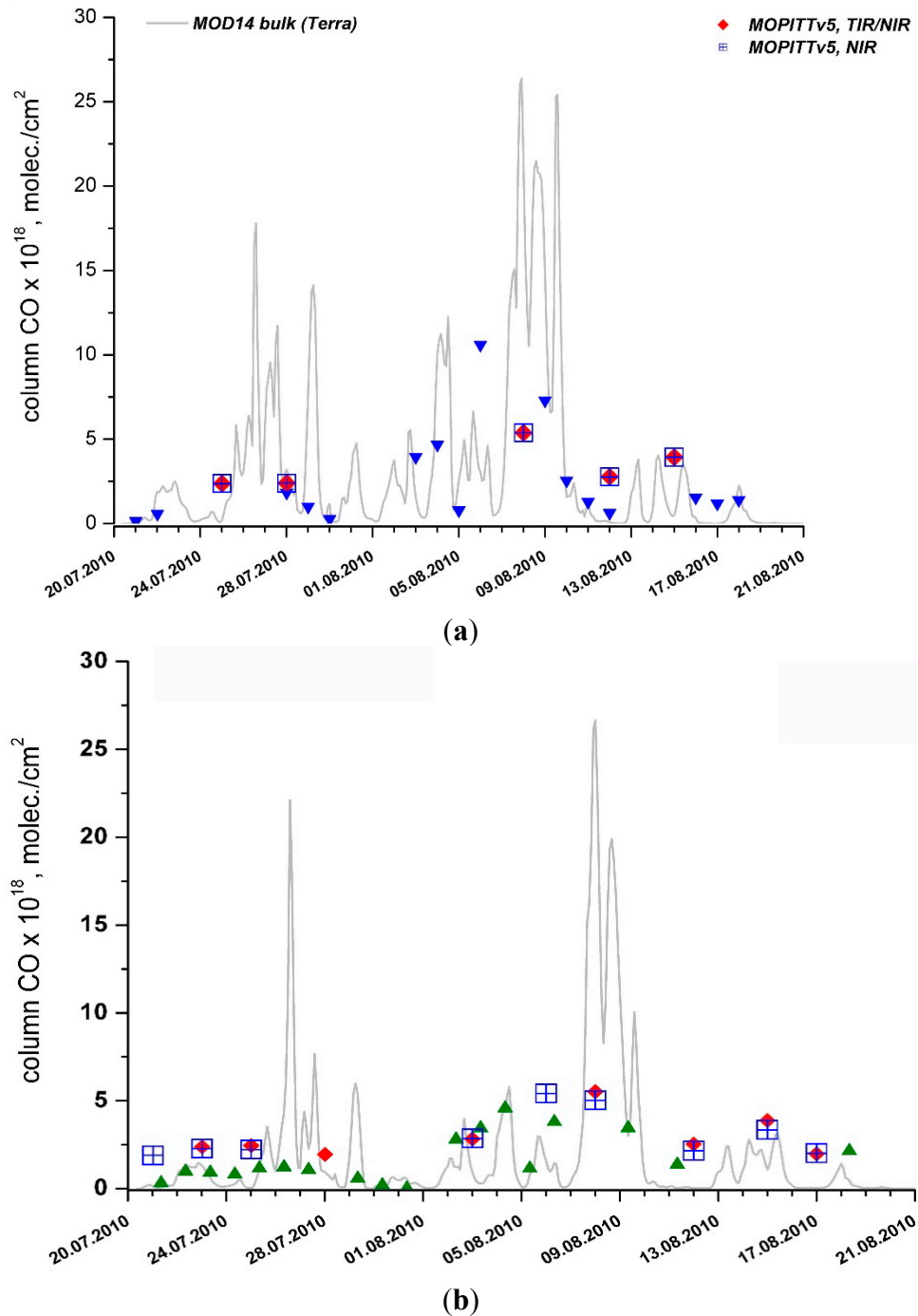

Figure 10. Experimental for OIAP (**a**) and ZSS (**b**) stations CO total columns and retrieval total column for MOPITTv5 NIR-only, MOPITTv5 TIR/NIR and MOPITTv4 satellite data have been shown. The model (RAMS/HYPACT) CO total column for MODIS/Terra hot spots has been shown as background for comparison.

As a summary, we can conclude that all three sensors, MOPITT/Terra, AIRS/Aura and IASI/MetOp, showed low sensitivity in the lower troposphere. A MOPITT-Team attempted to improve the sensitivity of the sensor by using a multi-spectral method in the signal processing. Their results look promising. However, a comparison between the MOPITTv5 TIR/NIR (NIR-only) and the experimental values showed the absolute values were lower than the measurements.

In this regard, we suggest orbit optimization for satellites that perform spectrometer measurements. During satellite measurement, the satellite orbit must be synchronized with the Earth's rotation around the sun so that the PBL height has a maximum value under the satellite in nadir. Thus, the authors recommend that sensors such as the MOPITT, AIRS and IASI not be placed on the same satellite platforms that the MODIS sensors were placed because the MODIS requires different orbital characteristics.

5. Discussion

5.1. Fire Emission Inventories Comparisons

In this section, the CO emission calculated by the emission sub-model described above (see Equations (1) and (2)), was compared with the recently developed fire emission inventories: FINNv1, 2011 (Fire INventory from NCAR), GFEDv3.1, 2010 (Global Fire Emissions Database) and GFASv1, 2011 (Global Fire Assimilation System).

The FINNv1 dataset has a spatial resolution 1 × 1 km and a daily time step. This dataset includes global emissions from forest fires, grassland and steppe burning, but does not include waste burned and emissions from wood used as biofuel [87,88]. The FINNv1 is the next stage of bulk method development [5]. The fire positions were defined by use of the MOD14/MYD14 orbital data obtained by the Terra and Aqua satellites. The FRP (Fire Radiative Power) parameterization was not used in the process of FINNv1 dataset creation. This FINNv1 dataset (combined data from Aqua and Terra satellites) excludes double counting of the same hot spots, which were recorded during one day by both satellites [89]. The vegetation density was based on the MODIS VCF (Vegetation Continuous Fields), Collection 3, 2001. The vegetation map was derived from the MODIS Collection 5 Land Cover Type (LCT) with 16 categories of IGBP classification [90]. For details see [87].

The GFEDv3.1 fire emission inventory includes three datasets: burned areas [61], monthly emission [66] and daily emission [91]. The GFEDv3.1 monthly emission has a spatial resolution of 0.5° × 0.5°. The Carnegie-Ames-Stanford-Approach (CASA) biochemical model and the satellite-based burned areas data were used in the process of creating the GFEDv3.1 dataset. The MCD45/MODIS burned areas product was used for the period 2001 to 2011, and the TRMM (Tropical Rainfall Measuring Mission), the VIRS (Visible and Infrared Scanner) and the ATSR (Along-Track Scanning Radiometer) satellite products were used to define the burned areas for the period of 1997 to 2000. A more detailed description of the GFEDv3.1 emission sub-model and the differences from the previous GFEDv2 version can be found in [66]. In this study, we used the daily GFEDv3.1 version [91]. This dataset was received from the monthly GFEDv3.1 version by splitting data with a synoptic and daily cycle and using the infrared channels of the MODIS data (product MOD14/MYD14).

The third fire emission inventory used for comparison is the GFASv1 [92]. This dataset is derived from recorded T21 and T31 radiative temperatures. This GFASv1 dataset is the next step in the

development of the FRP method, which is described in [60]. The GFASv1 dataset has a 0.5° × 0.5° spatial resolution, a daily periodicity and covers the period from 2003 to 2011. Spatial hot spot positions could be determined in real time (*i.e.*, the dataset could be operational). The detailed description can be found in [92].

The CO emissions from the FINNv1, GFEDv3.1 and GFASv1 data from the investigated regions around Moscow are shown in Figure 11. The grey color in Figure 11 corresponds to the peat bogs located near Moscow [4]. The peat bogs percentage of the total emission was defined by the hot spot positions (not by the categories of the GLC-2000 land cover map). The total emission and emission from the peat bog areas are presented in Table 1. Figure 11 and Table 1 demonstrate the differences between the FINNv1, GFEDv3.1, and GFASv1 emission data. The GFASv1 dataset exhibits a maximum of approximately 2 Tg/day. Furthermore, the fraction of peat bogs emission is approximately 75%. The GFEDv3.1 and FINNv1 datasets show lower emission values, which do not exceed 0.2 and 0.3 Tg/day, respectively.

The original FRP method without any corrections (GFASv1, see description) results in low values of approximately 0.3 Tg/day for Terra (MOD14 FRP) and Aqua (MYD14 FRP), see Figure 12a. The emission calculated with the MCD45 method of localization reaches a maximum of approximately 0.6 Tg/day, which is more than is derived from the GFEDv3.1. The percentage of peat bogs from the MCD45 method, approximately 20%, was the lowest that can be expected. Note that from space, the color of the Earth's surface covered with peat bogs looks similar to the color of vegetation damaged by fires, see Figure 12b.
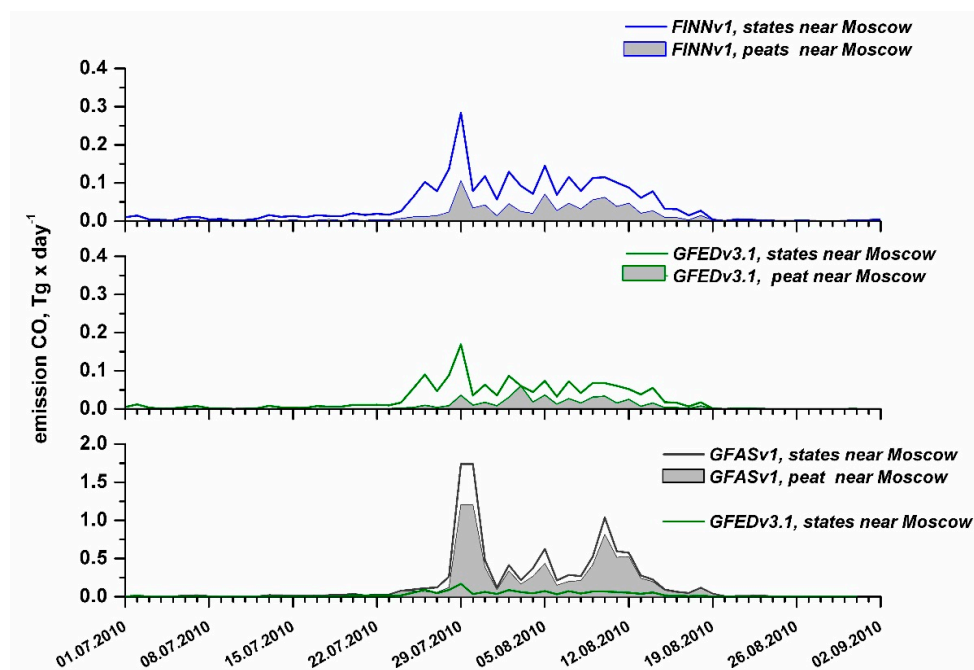

Figure 11. Daily CO emissions from wildfires in the central part of Russian plain between 1 July 2010 and 1 September 2010. The emission values are taken from FINNv1, GFEDv3.1 and GFASv1 datasets. The grey background color corresponded to peat areas (hatch areas in Figure 1c).

CO emissions calculated for MOD14/MYD14 hot spots localization by Equation (1) are shown in Figure 13. The dotted line represents the result for GFASv1 emission in peat areas, which is given for comparison. Note that a calculation for peat area of the MOD14/MYD14 bulk emission (grey color filled plot) is in close agreement with the GFASv1 inventory data (dotted line). The total emission calculated by MOD14/MYD14 bulk method (13.58/12.13 Tg) look the same as GFASv1 inventory value (8.37 Tg) for peat areas (see Table 1). However on the territory out of peat the total emission values of the FINNv1 (1.69 Tg), GFEDv3.1 (1.08 Tg) and partly GFASv1 (2.7 Tg) (see column "Difference", Table 1) are in agreement with MOD14/MYD14 FRP (1.48/1.19 Tg) emission values.

As shown above, the GFASv1 dataset resulted in a larger value of emission compared to the GFEDv3.1 and FINNv1 datasets.
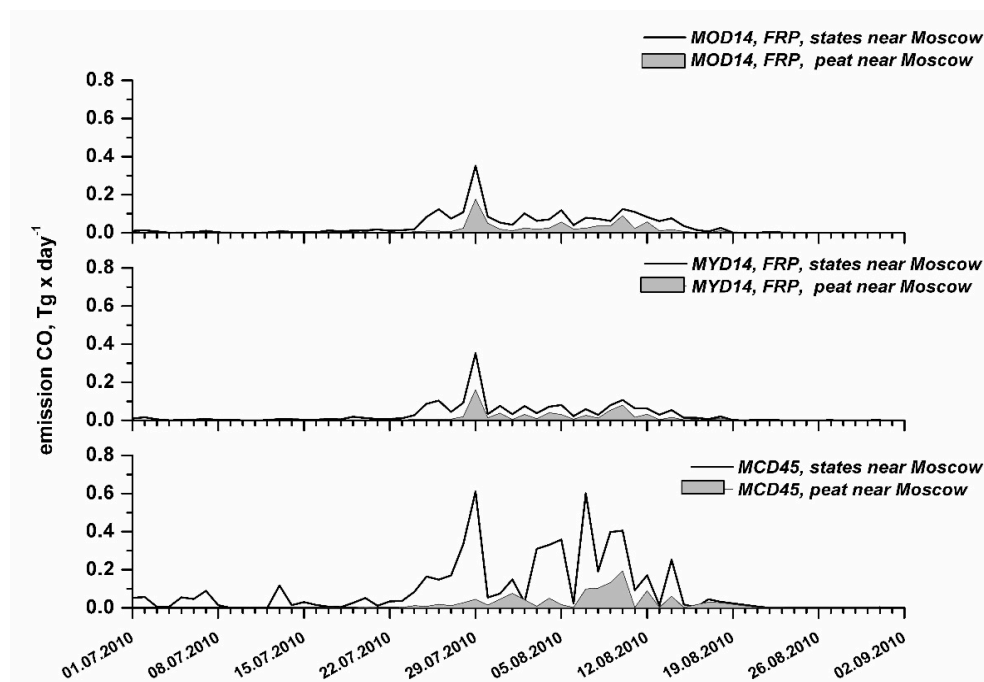

Figure 12. Daily CO emissions from wildfires in the central part of Russian plain between 1 July and 1 September, 2010. The emission values were calculated by FRP method (Equation (2)) with ignition localization by orbital data of MOD14 (Terra) и Aqua (MYD14) and by "Burned area" bulk method (Equation (1)) with ignition localization based on MCD45A1 data. The grey background color corresponds to peat areas (hatch areas in Figure 1c).

On the other hand, as shown in [13], the GFASv1, as the emission sub-model for the IFS-TM5, which is coupled Integrated Forecast System (operational global meteorological forecasting model) with Tracer Model version 5 (chemistry transport model) [93], underestimates the CO total column in comparison with the MOPITT v4 data. Total emissions for all considered methods are shown in Table 1. In addition, peat fires emissions and their percentages are specified. Possibility to use different scenarios as emission submodel for air quality forecasting system was specified in Table 1 in additional.

Summarizing the results from this section, it is possible to note that according to independent studies the total CO emissions varieties are in range from 1.53 Tg (GFEDv3.1) to 11.07 Tg (GFASv1). Our calculations also show that the total varieties of emissions are in a wide range (1.85–35.32 Tg

depending on the calculation methods). This point clearly indicates a necessity to perform the further work for the improvement of wildfire emission calculation methods. The question of the suitability of FRP method (Equation (2)) for calculation of emissions from peat areas remains controversial. The MODIS detection algorithm is not tuned to look for the small temperature changes in the overlying soil that is characteristic of peat fires. Therefore, the algorithm probably gives us only localization of such fires, but does not provide us any information about emission rate.
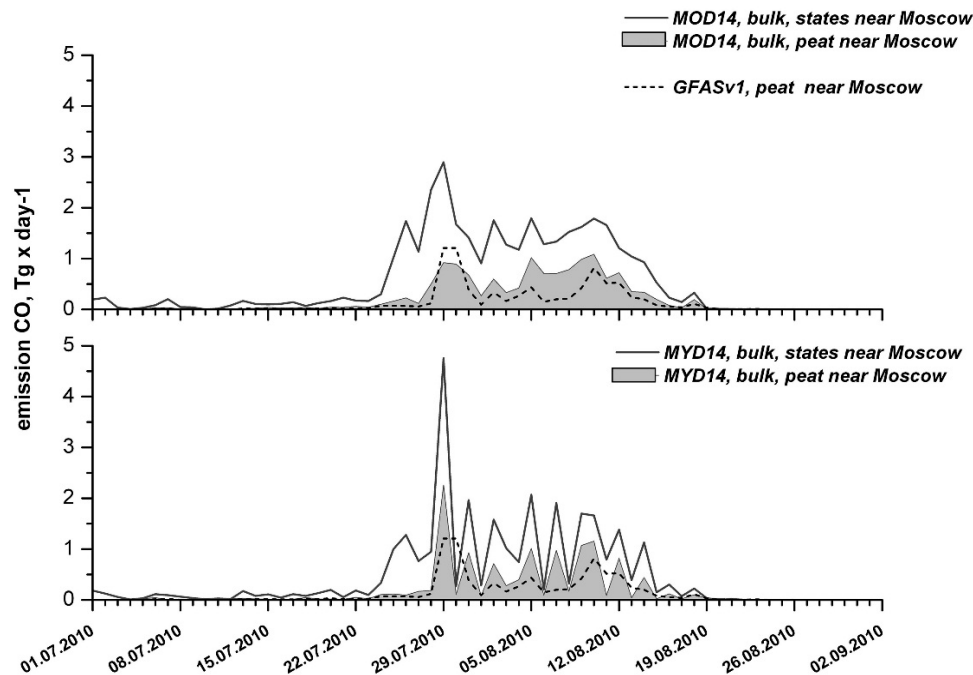

Figure 13. Daily CO emissions from wildfires in the central part of Russian plain and peat areas (grey background color) between 1 July and 1 September, 2010. The emission values were calculated by "bulk method" (Equation (1)) with ignition localization by MOD14/MYD14 data. The GFASv1 emission values in peat area have been shown as dash line in the figure for comparison.

5.2. Comparison of This Study Emission Inventories with the TM5-4DVAR Chemistry Transport Model Simulation

We compare our results with those from [7], which have been obtained by using the TM5-4DVAR system in combination with CO column observations of the Infrared Atmospheric Sounding Interferometer (IASI) for R1 and R2 regions.R1 region is defined from 35°E to 45°E and from 53°N to 58°N, so the R1 region is a bit less than a central part of Russian plain, is shown in (Figure 1b.). R2 region is defined from 30°E to 70°E and from 46°N to 70°N and it is approximately corresponded to the domain I in (Figure 1a). The total emission from Krol *et al.* [7] for R1 area before and after 4DVAR data assimilation with IASI data was by added in last two rows in Table 1 for discussion.

The 4DVAR assimilation procedure increased a value of GFED3 in 16 times from 0.63 Tg to 10.06 Tg and slightly reduced a value of GFAS from 10.52 Tg to 9.93 Tg (see Table 1).

However in the case of R2 region, which is approximately the same in size as a domain-I in this study, TM5-4DVAR model after assimilation of IASI data suddenly, without any the objective

reasons, rose up emission in 11 times (from 2.00 Tg to 22.30 Tg) for GFED3 inventory and in 1.8 times (from 12.40 Tgto 22.00 Tg) for GFAS inventory. As a result, the TM5-4DVAR model indicated that most of CO emissions were due to burning of none peat territories(see Figure 3 in [7]). It is difficult to explain how the combustion of shrub and grassland vegetation outside the R1 region could result in a large amount of CO emissions. Therefore, we think there are no bases to put under doubts 3.04 Tg (GFED) and 1.88 Tg (GFAS) prior emissions in the (R2-R1) area.

In addition, due to the removal of effective sources of emissions from the Moscow area, the TM5-4DVAR model will significantly underestimate the CO concentrations in Moscow. Indeed, as in the upper panel of Figure 5 of [7], the after IASI assimilation simulated values were ten times lower than the experimental data (logarithmic scale in Figure 5).

On the other side, the TM5-4DVAR emission are closer to the inventory estimations of the MOD14/bulk (35.32 Tg) and the MYD14/bulk (29.29 Tg) (see Table 1).

A simple diagram illustrated a situation when the emission date after IASI assimilation of wildfire emission shifted in the (R2-R1) region (Figure 14). For discussion three positions are allocated in Figure 14. The position (1) represents an area in which the convection and turbulence processes were strongly suppressed due to aerosol presence, PBL $<h_{sl}$. The position (2) is a region, where the certain amount of pollutions lifts up above a low sensitivity level due to the processes of intensive mixing of pollutions, and the satellite is able to perform well recording of pollutions above h_{sl} level. The third position (3) corresponds to a region, in which pollution is lifting up additionally due to the topography (Ural Mountains). We note, that the average kernels reaches a maximum at the heights 400–500 hPa, see for more details in [6].
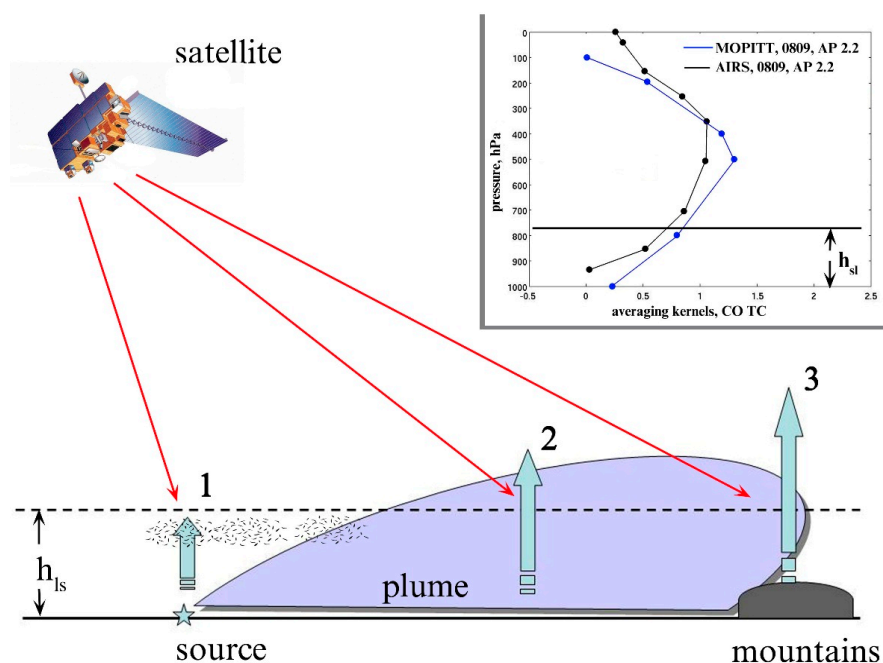

Figure 14. The scheme explained why the satellite sensitivity depends on satellite scanning locations. Dashed line shows the h_{sl} level, below which the satellite sensor MOPITT has a low sensitivity; $h_{sl}\sim 2$ km. A PBL values are shown as blue arrows. On the plate the typical average kernels of CO total column for MOPITT and AIRS sensors were shown in additional.

Nearby peat fires the aerosol suppressed the convective and turbulent processes in atmosphere, so the plume does not reach the top of satellite sensor sensitivity layer (h_{ls}). The satellite sensor, scanning the area nearby peat fires (position 1 in Figure 14), couldn't find out any contaminations both in the surface layer and in column. Note that the aerosol itself has no effect on carbon monoxide recording in TIR and NIR range. In other words, it is possible to confirm that satellite sensitivity is strongly depended on PBL.

With increasing distance from a peat fires area, the aerosol density in the lower troposphere decreased, the mixing processes grown and the plume reached the lower limit of satellite sensitivity (position 2 in Figure 14). The satellite recorded the part of plume, which was located above h_{ls} level. Additional mixing of the atmosphere occurs due to perturbations when the atmospheric mass passed over the Ural Mountains (position 3 in Figure 14). The spatial distribution for IASI CO TC is presented in (Figure1, [7]).

At the end of this section, we make some conclusions. From one side, as demonstrated in [7], the CO total emission for R2 region rose from 12.4 Tg for GFAS method (after adjustment for AERONET, [92]) to 22.0 Tg (after adjustment for TM5-4DVAR with IASI column data) what is close to our estimations of 29–35 Tg (by MOD14/MYD14/bulk methods). From the other side, the TM5-4DVAR method showed low emission values nearby the centers of peat combustion, and this confirmed our conclusion about low sensor sensitivity in case of the depressed vertical mixing.

6. Conclusions

In this study, the spatial and temporal distributions of the carbon monoxide (CO) emissions produced by forest and peat wildfires near Moscow during the abnormally hot summer of 2010 were investigated.

The wildfires in the summer of 2010 near Moscow have brought to light a number of problems.

First Problem: As it was shown in previous studies [4,6], the satellite sensors have low sensitivity to identify large quantity of carbon monoxide in the lower troposphere.

Result: In this study, the comparison between satellite MOPITT data (NIR, TIR and joint TIR/NIR channels) with the ground-based measurements, obtained at the OIPA and MSU stations, was performed. The CO total column data of MOPITTv5 NIR and TIR/NIR look more realistic than MOPITTv4 data, however the improvement in sensitivity by using NIR and NIR/TIR channels were less than it was to be expected.

The surface concentration measurements of carbon monoxide during wildfires period from the MOPITTv4 and MOPITTv5 were low, and these values did not show any consistency with the MSU, ZSS stations measurements.

A careful suggestion on satellite orbit optimization, which could allow to improve and to make more representative future spectrometric measurements, such as the MOPITT, AIRS and IASI measurements are given. The satellite should have an orbit that will correspond to the spatial strip with a maximum PBL in nadir (sun synchronized orbit). The expressed opinion is that future placement on the same platform devices, such as MODIS and MOPITT, which require different satellite orbit parameters, is inadvisable.

Second Problem: The second problem revealed accuracy of the wildfire emission inventories.

Result: According to independent studies the total CO emissions varieties are in the range of 1.53 Tg (GFEDv3.1) to 11.07 Tg (GFASv1). Our calculations also have shown that depending on the calculation methods, the total emissions can change in a wide range (1.85–35.32 Tg). It is shown that in this particular case the CO emission, calculated by different standard methods (Equation (1)) and (Equation (2)) for rapid AF product MOD14/MYD14, can differ by more than 15 times (See Table 1). The possibility of using FRP techniques for estimation of peat fires emissions is controversial. The MODIS detection algorithm is not tuned to detect the small temperature changes in the overlying soil layers, which are typical for coal and peat fires. Therefore, MODIS algorithm probably gives only a localization of such fires, but does not provide us any information about an emission rate.

Third Problem: The lack of operational forecast distributions of contaminants for large fires had a negative impact on the health of the population of the Moscow metropolitan area. In this study, we tested RAMS/HYPACT dispersion model as operative forecast model for purposes of air quality.

Result: The RAMS/HYPACT model results were compared with the CO surface concentrations measured at the MSU and ZSS stations. The model underestimated the concentration of carbon monoxide by two times during the period of intensive peat fires. However, the comparison of the RAMS/HYPACT model results with the ground-based CO total column measured at the OIAP and ZSS stations showed that the model overestimated the ground-based CO column values by two to three times during the same period of wildfires. Thus, it is possible to conclude that the RAMS/HYPACT model predicts more intensive turbulent processes in the PBL during daylight hours than actually occur. The presence of enormous quantities of wildfire aerosols, which could not be considered in a model, was a reason for this disagreement between simulation and practice. This conclusion agrees with that of [7]. Such a defect is a fault of all off-line dispersion models, which have not any aerosol-radiation feedbacks, see also [94–96].

A similar conclusion was made in [97], where it was specified that the Russian forest fire case study has shown significant aerosol direct effects on meteorology and high levels of PM_{10} over the Moscow area caused significantly reduced downward short wave radiation and also reduced PBL height.

Therefore, only limited applications of the off-line RAMS/HYPACT model as a forecasting air quality model are possible, and only in cases in which a wildfire aerosol does not suppress the convective and turbulent processes in atmosphere.

Acknowledgments

Author Contributions

Alexander N. Safronov designed the study, analyzed the data, made model simulations and wrote the manuscript. Ekaterina V. Fokeeva and Vadim S. Rakitin measured CO total columns at OIAP station, analyzed the data and wrote the manuscript. Eugene I. Grechko contributed to the study design and results discussion. Roman A. Shumsky measured CO concentrations and MTP-5 temperature profiles at MSU station.

Conflicts of Interest

The authors declare no conflict of interest.

References

1. Page, S.E.; Siegert, F.; Rieley, J.O.; Boehm, H.-D.V.; Jaya, A.; Limin, S.H. The amount of carbon released from peat and forest fires in Indonesia during 1997. *Nature* **2002**, *420*, 61–65.

2. Rein, G.; Cleaver, N.; Ashton, C.; Pironi, P.; Torero, J. The severity of smouldering peat fires and damage to the forest soil. *Catena* **2008**, *74*, 304–309.

3. Chubarova, N.Y.; Prilepsky, N.G.; Rublev, A.N.; Riebau, A.R. A Mega-fire event in central Russia: Fire weather, radiative, and optical properties of the atmosphere, and consequences for subboreal forest plants. *Dev. Environ. Sci.* **2008**, *8*, 247–264.

4. Fokeeva, E.V.; Safronov, A.N.; Rakitin, V.S.; Yurganov, L.N.; Grechko, E.I.; Shumskii, R.A. Investigation of the 2010 July–August fires impact on carbon monoxide atmospheric pollution in Moscow and its outskirts, estimating of emissions. *Izv. Atmos. Ocean. Phys.* **2011**, *47*, 682–698.

5. Wiedinmyer, C.; Quayle, B.; Geron, C.; Belote, A.; McKenzie, D.; Zhang, X.; O'Neill, S.; Wynne, K.K. Estimating emissions from fires in North America for air quality modeling. *Atmos. Environ.* **2006**, *40*, 3419–3432.

6. Yurganov, L.N.; Rakitin, V.; Dzhola, A.; August, T.; Fokeeva, E.; George, M.; Gorchakov, G.; Grechko, E.; Hannon, S.; Karpov, A.; *et al.* Satellite- and ground-based CO total column observations over 2010 Russian fires: Accuracy of top-down estimates based on thermal IR satellite data. *Atmos. Chem. Phys.* **2011**, *11*, 7925–7942.

7. Krol, M.; Peters, W.; Hooghiemstra, P.; George, M.; Clerbaux, C.; Hurtmans, D.; McInerney, D.; Sedano, F.; Bergamaschi, P.; El Hajj, M.; *et al.* How much CO was emitted by the 2010 fires around Moscow? *Atmos. Chem. Phys.* **2013**, *13*, 4737–4747.

8. Elansky, N.F.; Mokhov, I.I.; Belikov, I.B.; Berezina, E.V.; Elokhov, A.S.; Ivanov, V.A.; Pankratova, N.V.; Postylyakov, O.V.; Safronov, A.N.; Skorokhod, A.I.; *et al.* Gaseous admixtures in the atmosphere over Moscow during the 2010 summer. *Izv.Atmos. Ocean. Phys.* **2011**, *47*, 672–681.

9. Elansky, N.F.; Mokhov, I.I.; Belikov, I.B.; Berezina, E.V.; Elokhov, A.S.; Ivanov, V.A.; Pankratova, N.V.; Postylyakov, O.V.; Safronov, A.N.; Skorokhod, A.I.; *et al.* Gas composition of the surface air in Moscow during the extreme summer of 2010. *Dokl. Earth Sci.* **2011**, *437*, 357–362.

10. Bondur, V.G. The urgency and the need for space monitoring of natural fires in Russia. *Vestn. Otd. Nauk Zemle RAN* **2010**, *2*, 1–16.

11. Konovalov, I.B.; Beekmann, M.; Kuznetsova, I.N.; Yurova, A.; Zvyagintsev, A.M. Atmospheric impacts of the 2010 Russian wildfires: Integrating modelling and measurements of an extreme air pollution episode in the Moscow region. *Atmos. Chem. Phys.* **2011**, *11*, 10031–10056.

12. Witte, J.C.; Douglass, A.R.; da Silva, A.; Torres, O.; Levy, R.; Duncan, B.N. NASA A-Train and Terra observations of the 2010 Russian wildfires. *Atmos. Chem. Phys.* **2011**, *11*, 9287–9301.

13. Huijnen, V.; Flemming, J.; Kaiser, J.W.; Inness, A.; Leitão, J.; Heil, A.; Eskes, H.J.; Schultz, M.G.; Benedetti, A.; Dufour, G.; *et al.* Hindcast experiments of tropospheric composition during the summer 2010 fires over Western Russia. *Atmos. Chem. Phys.* **2012**, *12*, 4341–4364.

14. R'Honi, Y.; Clarisse, L.; Clerbaux, C.; Hurtmans, D.; Duflot, V.; Turquety, S.; Ngadi, Y.; Coheur, P.F. Exceptional emissions of NH_3 and HCOOH in the 2010 Russian wildfires. *Atmos. Chem. Phys.* **2013**, *13*, 4171–4181.

15. Safronov, A.N.; Fokeeva, E.V.; Rakitin, V.S.; Yurganov, L.N.; Grechko, E.I. Carbon monoxide emissions in summer 2010 in the central part of the Russian plain and estimation of their uncertainties with the use of different land cover maps. *Izv. Atmos. Ocean. Phys.* **2012**, *48*, 926–943.

16. Atmospheric Infrared Sounder (AIRS). Available online: http://disc.sci.gsfc.nasa.gov/AIRS/additional/instruments.shtml (accessed on 19 December 2014).

17. Measurement of Pollution in the Troposphere (MOPITT). Available online: http://www2.acd.ucar.edu/mopitt (accessed on 19 December 2014).

18. Infrared Atmospheric Sounding Interferometer (IASI). Available online: http://www.esa.int/Our_Activities/Observing_the_Earth/The_Living_Planet_Programme/Meteorological_missions/MetOp/About_IASI (accessed on 19 December 2014).

19. Deeter, M.N.; Worden, H.M.; Edwards, D.P.; Gille, J.C.; Andrews, A.E. Evaluation of MOPITT retrievals of lower-tropospheric carbon monoxide over the United States. *J. Geophys. Res.* **2012**, *117*, doi:10.1029/2012JD017553.

20. Deeter, M.N.; Martínez-Alonso, S.; Edwards, D.P.; Emmons, L.K.; Gille, J.C.; Worden, H.M.; Pittman, J.V.; Daube, B.C.; Wofsy, S.C. Validation of MOPITT version 5 thermal-infrared, near-infrared, and multispectral carbon monoxide profile retrievals for 2000–2011. *J. Geophys. Res.* **2013**, *118*, 6710–6725.

21. Deeter, M.N. Measurements of Pollution in the Troposphere (MOPITT), Version 6 Product User's Guide. Available online: http://www2.acd.ucar.edu/sites/default/files/mopitt/v6_users_guide_201309.pdf (accessed on 19 December 2014).

22. Revich, B. Heat-wave, air quality and mortality in the Russian Federation's Europe, 2010: Preliminary assessment. *Hum. Ecol.* **2011**, *7*, 3–9.

23. Revich, B.A.; Shaposhnikov, D.A. Climate change, heat waves, and cold spells as risk factors for increased mortality in some regions of Russia. *Stud. Russ. Econ. Dev.* **2012**, *23*, 195–207.

24. TE48 Description, Thermo Electron Corp/Formerly Thermo Environmental Instruments Inc. Available online: http://www.thermoscientific.com/en/product/model-48-i-i-i-co-analyzer.html (accessed on 19 December 2014).

25. Dianov-Klokov, V.; Yurganov, L.; Grechko, E.; Dzhola, A. Spectroscopic measurements of atmospheric carbon monoxide and methane. 1: Latitudinal distribution. *J. Atmos. Chem.* **1989**, *8*, 139–151.

26. Fokeeva, E.; Grechko, E.; Dzhola, A.; Rakitin, V. Determination of carbon monoxide pollution of the atmosphere over Moscow with a spectroscopic method. *Izv. Atmos. Ocean. Phys.* **2007**, *43*, 612–617.

27. McKernan, E.; Yurganov, L.N.; Tolton, B.T.; Drummond, J.R. MOPITT validation using ground-based IR spectroscopy. *Proc. SPIE* **1999**, *3756*, 486–491.

28. Yurganov, L.; Grechko, E.; Dzhola, A. Long-term measurements of carbon monoxide over Russia using a spectrometer of medium resolution. *Recent Res. Dev. Geophys.* **2002**, *4*, 249–265.

29. Deeter, M.; Emmons, L.; Francis, G.; Edwards, D.; Gille, J.; Warner, J.; Khattatov, B.; Ziskin, D.; Lamarque, J.; Ho, S. Operational carbon monoxide retrieval algorithm and selected results for the MOPITT instrument. *J. Geophys. Res* .**2003**, *108*, doi:10.1029/2002JD003186.

30. Deeter, M.N.; Edwards, D.P.; Gille, J.C.; Emmons, L.K.; Francis, G.; Ho, S.P.; Mao, D.; Masters, D.; Worden, H.; Drummond, J.R.; *et al.* The MOPITT version 4 CO product: Algorithm enhancements, validation, and long-term stability. *J. Geophys. Res.* **2010**, *115*, doi:10.1029/2009JD013005

31. OPeNDAP Hyrax (1.6.2), Products: MOP03J.005, MOP03N.005, MOP03T.005. Available online: http://l0dup05.larc.nasa.gov/opendap/MOPITT/ (accessed on 19 December 2014).

32. The RAMS HYbrid Particle and Concentration Transport Model (HYPACT). Available online: http://www.atmet.com/ (accessed on 19 December 2014).

33. Seinfeld, J.H.; Pandis, S.N. *Atmospheric Chemistry and Physics: From Air Pollution to Climate Change*; John Wiley and Sons: New York, NY, USA, 1998.

34. Pielke, R.A.; Cotton, W.R.; Walko, R.L.; Tremback, C.J.; Lyons, W.A.; Grasso, L.D.; Nicholls, M.E.; Moran, M.D.; Wesley, D.A.; Lee, T.J.; *et al.* A comprehensive meteorological modeling system—RAMS. *Meteorol. Atmos. Phys.* **1992**, *49*, 69–91.

35. Walko, R.L.; Cotton, W.; Meyers, M.; Harrington, J. New RAMS cloud microphysics parameterization part I: The single-moment scheme. *Atmos. Res.* **1995**, *38*, 29–62.

36. Cotton, W.R.; Pielke, R., Sr.; Walko, R.; Liston, G.; Tremback, C.; Jiang, H.; McAnelly, R.; Harrington, J.; Nicholls, M.; Carrio, G. RAMS 2001: Current status and future directions. *Meteorol. Atmos. Phys.* **2003**, *82*, 5–29.

37. National Center for Environmental Predictions (NCAR/NCEP). Available online: http://dss.ucar.edu/datasets (accessed on 15 December 2011).

38. Topography in Metres (a.s.l.), the 30 Seconds Resolution (GTOPO30), USGS, (U.S. Geological Survey). Available online: http://eros.usgs.gov/#/Find_Data/Products_and_Data_Available/ gtopo30_info (accessed on 15 December 2011).

39. Walko, R.L.; Band, L.E.; Baron, J.; Kittel, T.G.F.; Lammers, R.; Lee, T.J.; Ojima, D.; Pielke, R.A.; Taylor, C.; Tague, C.; *et al.* Coupled atmosphere-biophysicshydrology models for environmental modeling. *J. Appl. Meteorol.* **2000**, *39*, 931–944.

40. Chen, C.; Cotton, W.R. A one-dimensional simulation of the stratocumulus-capped mixed layer. *Bound. Layer Meteorol.* **1983**, *25*, 289–321.

41. Kuo, H.L. Further studies of the parameterization of the influence of cumulus convection on large-scaleflow. *J. Atmos.Sci.* **1974**, *31*, 1232–1240.

42. Meyers, M.P.; Walko, R.L.; Harrington, J.Y.; Cotton, W.R. New RAMS cloud microphysics parameterization. Part II: The two-moment scheme. *Atmos. Res.* **1997**, *45*, 3–39.

43. Smagorinsky, J. General circulation experiments with the primitive equations. *Mon. Weather Rev.* **1963**, *91*, 99–164.

44. Mellor, G.L.; Yamada, T. A hierarchy of turbulence closure models for planetary boundary layers. *J. Atmos. Sci.* **1974**, *31*, 1791–1806.

45. Mellor, G.L.; Yamada, T. Development of a turbulence closure model for geophysical fluid problems. *Rev. Geophys. Space Phys.* **1982**, *20*, 851–875.

46. Klemp, J.B.; Wilhelmson, R.B. The simulation of three-dimensional convective storm dynamics. *J. Atmos. Sci.* **1978**, *35*, 1070–1096.

47. Benjamin, S.G.; Grell, G.A.; Brown, J.M.; Smirnova, T.G.; Bleck, R. Mesoscale weather prediction with the RUC hybrid isentropic/terrain-following coordinate model. *Mon. Weather Rev.* **2004**, *132*, 473–494.

48. Devenyi, D.; Benjamin, S.G. A 3-dimensional atmospheric variational assimilation technique in a hybrid isentropic-sigma coordinate. *Meteorol. Atmos. Phys.* **2003**, *82*, 245–257.

49. HYbrid Particle and Concentration Transport Model, (HYPACT), Version 1.5, User's Guide. Available online: http://www.atmet.com/html/docs/hypact/1.5/hyp15_namelist-1.0.pdf (accessed on 19 December 2014).

50. Hurley, P.; Physick, W. A skewed homogeneous Lagrangian particle model for convective conditions. *Atmos. Environ. Part A Gen. Top.* **1993**, *27*, 619–624.

51. An, X.Q.; Chen, Y.C.; Lu, S. Estimation of winter TSP permissible total discharge amount in Lanzhou City. *China Environ. Sci.* **2003**, *23*, 60–63. (In Chinese)

52. Totten, L.A.; Stenchikov, G.; Gigliotti, C.L.; Lahoti, N.; Eisenreich, S.J. Measurement and modeling of urban atmospheric PCB concentrations on a small (8 km) spatial scale. *Atmos. Environ.* **2006**, *40*, 7940–7952.

53. Stenchikov, G.; Lahoti, N.; Diner, D.J.; Kahn, R.; Lioy, P.J.; Georgopoulos, P.G. Multiscale plume transport from the collapse of the world trade center on 11 September 2001. *Environ. Fluid Mech.* **2006**, *6*, 425–450.

54. Sathitkunarat, S.; Wongwises, P.; Pan-Aram, R.; Zhang, M. Carbon monoxide emission and concentration models for Chiang Mai urban area. *Adv. Atmos. Sci.* **2006**, *23*, 901–908.

55. Gangoiti, G.; Albizuri, A.; Alonso, L.; Navazo, M.; Matabuena, M.; Valdenebro, V.; García, J.; Millán, M. Sub-continental transport mechanisms and pathways during two ozone episodes in northern Spain. *Atmos. Chem. Phys.* **2006**, *6*, 1469–1484.

56. An, X.; Zuo, H.; Chen, L. Atmospheric environmental capacity of SO_2 in winter over Lanzhou in China: A case study. *Adv. Atmos. Sci.* **2007**, *24*, 688–699.

57. Pimonsree, S.; Wongwises, P.; Pan-Aram, R.; Zhang, M. Model analysis of PM_{10} concentration variations over a mineral products industrial area in Saraburi, Thailand. *Water Air Soil Pollut.* **2008**, *201*, 239–251.

58. Kido, H.; Fujiwara, H.; Jamsran, U.; Endo, A. The simulation of long-range transport of ^{137}Cs from East Asia to Japan in 2002 and 2006. *J. Environ. Radioact.* **2012**, *103*, 7–14.

59. Benjamin, S.G.; Devenyi, D.; Weygandt, S.S.; Brundage, K.J.; Brown, J.M.; Grell, G.A.; Kim, D.; Schwartz, B.E.; Smirnova, T.G.; Smith, T.L.; *et al.* An hourly assimilation-forecast cycle: The RUC. *Mon. Weather Rev.* **2004**, *132*, 495–518.

60. Wooster, M.J.; Roberts, G.; Perry, G.L.W.; Kaufman, Y.J. Retrieval of biomass combustion rates and totals from fire radiative power observations: FRP derivation and calibration relationships between biomass consumption and fire radiative energy release. *J. Geophys. Res.* **2005**, *110*, doi:10.1029/2005JD006318.

61. Giglio, L.; Randerson, J.T.; van der Werf, G.R.; Kasibhatla, P.S.; Collatz, G.J.; Morton, D.C.; DeFries, R.S. Assessing variability and long-term trends in burned area by merging multiple satellite fire products. *Biogeosciences* **2010**, *7*, 1171–1186.

62. Justice, C.; Giglio, L.; Korontzi, S.; Owens, J.; Morisette, J.; Roy, D.; Descloitres, J.; Alleaume, S.; Petitcolin, F.; Kaufman, Y. The MODIS fire products. *Remote Sens. Environ.* **2002**, *83*, 244–262.

63. Giglio, L.; Csiszar, I.; Justice, C.O. Global distribution and seasonality of active fires as observed with the Terra and Aqua Moderate Resolution Imaging Spectroradiometer (MODIS) sensors. *J. Geophys. Res.* **2006**, *111*, doi:10.1029/2005JG000142.

64. MODIS Collection 5 Active Fire Product. User's Guide Version 2.5. Available online: http://modis-fire.umd.edu/Documents/MODIS_Fire_Users_Guide_2.5.pdf (accessed on 20 December 2014).

65. MODIS Website. Available online: http://modis.gsfc.nasa.gov/about/specifications.php (accessed on 20 December 2014).

66. Van der Werf, G.R.; Randerson, J.T.; Giglio, L.; Collatz, G.J.; Mu, M.; Kasibhatla, P.S.; Morton, D.C.; DeFries, R.S.; Jin, Y.; van Leeuwen, T.T. Global fire emissions and the contribution of deforestation, savanna, forest, agricultural, and peat fires (1997–2009). *Atmos. Chem. Phys.* **2010**, *10*, 11707–11735.

67. Roy, D.; Boschetti, L.; Justice, C.; Ju, J. The collection 5 MODIS burned area product—Global evaluation by comparison with the MODIS active fire product. *Remote Sens. Environ.* **2008**, *112*, 3690–3707.

68. MODIS Collection 5 Burned Area Product-MCD45. Available online: https://earthdata.nasa.gov/sites/default/files/field/document/MODIS_Burned_Area_User_Guide_2.0.pdf (accessed on 20 December 2014).

69. Freitas, S.R.; Longo, K.M.; Chatfield, R.; Latham, D.; Silva Dias, M.A.F.; Andreae, M.O.; Prins, E.; Santos, J.C.; Gielow, R.; Carvalho, J.A., Jr. Including the sub-grid scale plume rise of vegetation fires in low resolution atmospheric transport models. *Atmos. Chem. Phys.* **2007**, *7*, 3385–3398.

70. Guan, H.; Esswein, R.; Lopez, J.; Bergstrom, R.; Warnock, A.; Follette-Cook, M.; Fromm, M.; Iraci, L.T. A multi-decadal history of biomass burning plume heights identified using aerosol index measurements. *Atmos. Chem. Phys.* **2010**, *10*, 6461–6469.

71. Longo, K.M.; Freitas, S.R.; Andreae, M.O.; Setzer, A.; Prins, E.; Artaxo, P. The coupled aerosol and tracer transport model to the Brazilian developments on the regional atmospheric modeling system (CATT-BRAMS)—Part 2: model sensitivity to the biomass burning inventories. *Atmos. Chem. Phys.* **2010**, *10*, 5785–5795.

72. Freitas, S.R.; Longo, K.M.; Alonso, M.F.; Pirre, M.; Marecal, V.; Grell, G.; Stockler, R.; Mello, R.F.; Sánchez Gácita, M. PREP-CHEM-SRC—1.0: A preprocessor of trace gas and aerosol emission fields for regional and global atmospheric chemistry models. *Geosci. Model Dev.* **2011**, *4*, 419–433.

73. Bartholomé, E.; Belward, A. GLC2000: A new approach to global land cover mapping from Earth observation data. *Int. J. Remote Sens.* **2005**, *26*, 1959–1977.

74. Bartalev, S.; Belward, A.; Erchov, D.; Isaev, A. A new SPOT4-VEGETATION derived land cover map of Northern Eurasia. *Int. J. Remote Sens.* **2003**, *24*, 1977–1982.

75. Global Land Cover 2000 Database. Available online: http://bioval.jrc.ec.europa.eu/products/glc2000/products.php (accessed on 19 December 2014).

76. Turquety, S.; Menut, L.; Bessagnet, B.; Anav, A.; Viovy, N.; Maignan, F.; Wooster, M. APIFLAME v1.0: High-resolution fire emission model and application to the Euro-Mediterranean region. *Geosci. Model Dev.* **2014**, *7*, 587–612.

77. Stockwell, C.E.; Yokelson, R.J.; Kreidenweis, S.M.; Robinson, A.L.; DeMott, P.J.; Sullivan, R.C.; Reardon, J.; Ryan, K.C.; Griffith, D.W.T.; Stevens, L. Trace gas emissions from combustion of peat, crop residue, domestic biofuels, grasses, and other fuels: Configuration and Fourier transform infrared (FTIR) component of the fourth Fire Lab at Missoula Experiment (FLAME-4). *Atmos. Chem. Phys.* **2014**, *14*, 9727–9754.

78. RLC Forest Stand Carbon Map of Russia. Data Set. Available online: http://daac.ornl.gov/cgi-bin/dsviewer.pl?ds_id=696 (accessed on 29 December 2014).

79. MERIS, GlobCover-2009. Available online: http://envisat.esa.int/earth/www/object/index.cfm?fobjectid=3762 (accessed on 19 December 2014).

80. Stolbovoi, V.; McCallum, I. *CD-ROM "Land Resources of Russia"*; International Institute for Applied Systems Analysis and the Russian Academy of Science: Laxenburg, Austria, 2002.

81. WMO Sounding Datasets. Available online: http://weather.uwyo.edu/upperair/sounding.html (accessed on 20 December 2014).

82. Microwave Temperature Profile Radiometer Description (MTP-5). Available online: http://attex.net/EN/mtp5HE.php (accessed on 19 December 2014).

83. Gridded Meteorological Data Archives (GDAS1 Dataset), Air Resources Laboratory, NASA, Available online: http://arlftp.arlhq.noaa.gov/pub/archives/gdas1 (accessed on 19 December 2014).

84. RAMS/HYPACT Evaluation and Visualization Utilities (REVU), User's Guide, Version 2.5. Available online: http://www.atmet.com/html/docs/revu/2.5/r25_namelist-1.0.pdf (accessed on 19 December 2014).

85. Grid Analysis and Display System (GrADS). Available online: http://www.iges.org/grads (accessed on 19 December 2014).

86. ArcInfo GIS System. Available online: http://www.esri.com/ (accessed on 19 December 2014).

87. Wiedinmyer, C.; Akagi, S.K.; Yokelson, R.J.; Emmons, L.K.; Al-Saadi, J.A.; Orlando, J.J.; Soja, A.J. The fire INventory from NCAR (FINN): A high resolution global model to estimate the emissions from open burning. *Geosci. Model Dev.* **2011**, *4*, 625–641.

88. Akagi, S.K.; Yokelson, R.J.; Wiedinmyer, C.; Alvarado, M.J.; Reid, J.S.; Karl, T.; Crounse, J.D.; Wennberg, P.O. Emission factors for open and domestic biomass burning for use in atmospheric models. *Atmos. Chem. Phys.* **2011**, *11*, 4039–4072.

89. Al-Saadi, J.; Soja, A.J.; Pierce, R.B.; Szykman, J.; Wiedinmyer, C.; Emmons, L.; Kondragunta, S.; Zhang, X.; Kittaka, C.; Schaack, T.; *et al.* Intercomparison of near-real-time biomass burning emissions estimates constrained by satellite fire data. *J. Appl. Remote Sens.* **2008**, *2*, 021504.

90. Friedl, M.A.; Sulla-Menashe, D.; Tan, B.; Schneider, A.; Ramankutty, N.; Sibley, A.; Huang, X. MODIS collection 5 global land cover: Algorithm refinements and characterization of new datasets. *Remote Sens. Environ.* **2010**, *114*, 168–182.

91. Mu, M.; Prins, E.M.; Griffith, D.W.T.; Wunch, D.; Toon, G.C.; Sherlock, V.J.; Wennberg, P.O.; Randerson, J.T.; van de Werf, G.R.; Giglio, L.; *et al.* Daily and 3-hourly variability in global fire emissions and consequences for atmospheric model predictions of carbon monoxide. *J. Geophys. Res.* **2011**, *116*, doi:10.1029/2011JD016245.

92. Kaiser, J.W.; Heil, A.; Andreae, M.O.; Benedetti, A.; Chubarova, N.; Jones, L.; Morcrette, J.J.; Razinger, M.; Schultz, M.G.; Suttie, M.; *et al.* Biomass burning emissions estimated with a global fire assimilation system based on observed fire radiative power. *Biogeosciences* **2012**, *9*, 527–554.

93. Huijnen, V.; Williams, J.; van Weele, M.; van Noije, T.; Krol, M.; Dentener, F.; Segers, A.; Houweling, S.; Peters, W.; de Laat, J.; *et al.* The global chemistry transport model TM5: Description and evaluation of the tropospheric chemistry version 3.0. *Geosci. Model Dev.* **2010**, *3*, 445–473.

94. Sofiev, M.; Vankevich, R.; Lotjonen, M.; Prank, M.; Petukhov, V.; Ermakova, T.; Koskinen, J.; Kukkonen, J. An operational system for the assimilation of the satellite information on wild-land fires for the needs of air quality modelling and forecasting. *Atmos. Chem. Phys.* **2009**, *9*, 6833–6847.

95. Kukkonen, J.; Olsson, T.; Schultz, D.M.; Baklanov, A.; Klein, T.; Miranda, A.I.; Monteiro, A.; Hirtl, M.; Tarvainen, V.; Boy, M.; *et al.* A review of operational, regional-scale, chemical weather forecasting models in Europe. *Atmos. Chem. Phys.* **2012**, *12*, 1–87.

96. Baklanov, A.; Schlünzen, K.; Suppan, P.; Baldasano, J.; Brunner, D.; Aksoyoglu, S.; Carmichael, G.; Douros, J.; Flemming, J.; Forkel, R.; *et al.* Online coupled regional meteorology chemistry models in Europe: Current status and prospects. *Atmos. Chem. Phys.* **2014**, *14*, 317–398.

97. Kong, X.; Forkel, R.; Sokhi, R.S.; Suppan, P.; Baklanov, A.; Gauss, M.; Brunner, D.; Baro, R.; Balzarini, A.; Chemel, C.; *et al.* Analysis of meteorology–chemistry interactions during air pollution episodes using online coupled models within AQMEII phase-2. *Atmos. Environ.* **2014,** in press.